

Modulational instability of Rossby and drift waves and generation of zonal jets

Colm Connaughton,^{1,2,*} Balasubramanya T. Nadiga,^{3,†} Sergey Nazarenko,^{2,‡} and Brenda Quinn^{2,§}

¹*Centre for Complexity Science, University of Warwick, Gibbet Hill Road, Coventry CV4 7AL, UK*

²*Mathematics Institute, University of Warwick, Gibbet Hill Road, Coventry CV4 7AL, UK*

³*Los Alamos National Laboratory, Los Alamos, New Mexico 87545, USA*

(Dated: November 8, 2018)

We study the modulational instability of geophysical Rossby and plasma drift waves within the Charney-Hasegawa-Mima (CHM) model both theoretically, using truncated (four-mode and three-mode) models, and numerically, using direct simulations of CHM equation in the Fourier space. The linear theory [1] predicts instability for any amplitude of the primary wave. For strong primary waves the most unstable modes are perpendicular to the primary wave, which correspond to generation of a zonal flow if the primary wave is purely meridional. For weaker waves, the maximum growth occurs for off-zonal inclined modulations. For very weak primary waves the unstable waves are close to being in three-wave resonance with the primary wave. The nonlinear theory [2] predicts that the zonal flows generated by the linear instability experience pinching into narrow zonal jets. Our numerical simulations confirm the theoretical predictions of the linear theory as well as of the nonlinear pinching. We find that, for strong primary waves, these narrow zonal jets further roll up into Karman-like vortex streets. On the other hand, for weak primary waves, the growth of the unstable mode reverses and the system oscillates between a dominant jet and a dominant primary wave. The 2D vortex streets appear to be more stable than purely 1D zonal jets, and their zonal-averaged speed can reach amplitudes much stronger than is allowed by the Rayleigh-Kuo instability criterion for the 1D case. We find that the truncation models work well for both the linear stage and often even for the medium-term nonlinear behavior. In the long term, the system transitions to turbulence helped by the vortex-pairing instability (for strong waves) and by the resonant wave-wave interactions (for weak waves).

PACS numbers: PACS go here

INTRODUCTION AND MOTIVATION

Zonal flows are prominent features in the atmospheres of giant planets such as Jupiter and Saturn [3, 4, 5], the Earth's atmosphere [6] and its oceans [5, 7]. Geophysical jets can regulate small-scale turbulence and transport processes via, for example, the “Barotropic Governor” mechanism [8]. Zonal flows are also important in plasma turbulence of fusion devices [9]. There, they can also regulate the turbulence and suppress transport via a drift-wave/zonal-flow feedback loop [10, 11]. The latter process is presently considered the main mechanism for the Low-to-High (LH) confinement transitions in tokamaks discovered in [12], - an effect which is crucial for the success of future fusion devices.

Two main zonal flow generation scenarios have been discussed in the literature. According to the first scenario zonal flows are generated via an inverse energy cascade, which could be local or nonlocal [10, 11]. The mechanism for such an inverse cascade is similar to that of 2D Navier-Stokes turbulence [13], but the presence of the beta-effect makes this cascade anisotropic. This leads to a preferential transfer of energy into zonal flows at large scales rather than into round vortices as would be the case in Navier-Stokes turbulence. The beta-effect leads to three-wave resonant interactions which preserve an additional (to the energy and the potential enstrophy) quadratic invariant, - zonostrophy [14, 15, 16]. Application of the

standard Fjørtoft argument to the three invariants, the energy, potential enstrophy and zonostrophy lead to the conclusion that the energy can only be transferred to large zonal scales [14]. This statistical argument is explained in detail in [17]. The second mechanism of zonal flow generation, and the principle topic of this article, is via modulational instability of a primary meridional Rossby/drift wave. In practice, such primary waves are themselves the result of an instability (typically the baroclinic instability in GFD or the ion-temperature-gradient instability in tokamaks) [1, 2, 18, 19, 20, 21, 22].

These mechanisms are unlikely to be exclusive in practice and both may coexist under some conditions. The extent to which one mechanism dominates over the other is determined by the parameter regime and configurational details. If the parameter regime were to be such that the baroclinic instability resulted in meridional Rossby waves, zonal flows would presumably result from the MI mechanism, whereas if the parameter regime were to be such that the baroclinic instability resulted in more isotropic eddies at the Rossby deformation radius, the cascade scenario would likely be more relevant. In our purely barotropic model, these effects are modeled by the initial condition. A narrow initial spectrum of the waves and large initial amplitude promotes the modulational instability mechanism leading to fast zonal flow generation bypassing the turbulent cascade stages. On the other hand, for broad initial spectra, the cascade scenario is

likely to be more relevant. There is an analogy with the turbulence of surface gravity waves on water where the inverse cascade and modulational (Benjamin-Fair) instability [23] can compete with each other in the generation of long waves [24]. A quantitative measure, called the Benjamin-Feir index, was suggested to estimate probability for triggering the modulational instability [24, 25]. Developing a similar approach for the Rossby/drift wave system would also be useful. However, we will leave this interesting subject for future studies, and in the present paper we will only be concerned with the modulational instability of a monochromatic wave.

We will start by revisiting the linear theory of the modulational instability which was first analysed by Loretz [18] and then treated in great detail in a beautiful paper by Gill [1]. Using numerical and semi-analytical calculations we highlight the most important properties of Gill's theory. In particular, we will see how the character of instability changes with the strength of the carrier wave: from being the classical hydrodynamic instability of the sinusoidal (Kolmogorov) shear flow for large amplitudes [26] to becoming a (three-wave) decay instability of weakly nonlinear waves for small amplitudes [27]. We will also study the effect of the finite Rossby/Larmor radius on the instability.

We will then proceed to study the nonlinear stage of the modulational instability with direct numerical simulations (DNS), comparing them with the solutions of the four-mode truncated (4MT) and the three-mode truncated (3MT) systems. We find that at the nonlinear stage, for strong primary waves, the growth of the zonal mode deviates from the truncated dynamics and the zonal flow tends to focus into narrow jets, as was theoretically predicted in [2]. These zonal jets subsequently become unstable and acquire the interesting two-dimensional structure of a double (Karman-like) vortex street. The vortex street appears to be more stable than a plane parallel shear flow with the same zonal profile [28] and persists for a relatively long time until (possibly due to dissipation) a vortex pairing instability sets in and triggers a transition to turbulence [28]. As the nonlinearity of the primary wave is decreased we find that there is a level of nonlinearity below which this sequence of events changes. For sufficiently weak primary waves, the jet strength reaches a maximum which is still stable. After this maximum is reached, the jet amplitude starts decreasing again, continuing to follow the truncated dynamics, and avoids the roll-up into vortices. This reversal of the jet growth, particularly the maximum jet strength, is well predicted by nonlinear oscillatory solutions of the 4MT, and often by the 3MT, equations. The latter are relevant for non-degenerate (in a sense which we shall explain) resonant wave triads. Once the full system deviates from the solutions of the truncated system, as it inevitably does, it sometimes continues to exhibit oscillatory behaviour for a while in the weak nonlinear-

ity cases. These subsequent oscillations have different periods, however, and are often rather irregular.

Along the way, we will examine the relative performance of the 3MT vs 4MT models thereby clarifying possible confusions on whether the principal mechanism of the modulational instability is 3-wave or 4-wave.

THE MODEL

Geophysical and plasma zonal flows are often mentioned together because of the same simplified nonlinear PDE which was suggested for their description, namely, the Charney-Hasegawa-Mima (CHM) equation [29, 30]:

$$\partial_t (\Delta\psi - F\psi) + \beta\partial_x\psi + J[\psi, \Delta\psi] = \nu_n(-\Delta)^n\psi, \quad (1)$$

where ψ is the streamfunction, $F = 1/\rho^2$ with ρ being the deformation radius in the GFD context and the ion Larmor radius in the plasma context, β is a constant proportional to the gradient of the horizontal rotation frequency or of the plasma density in the GFD and plasma contexts respectively. We introduced notation for the Jacobean operator,

$$J[f, g] = (\partial_x f)(\partial_y g) - (\partial_y f)(\partial_x g). \quad (2)$$

In the GFD context, the x -axis is in the west-east and the y -axis is along the south-north directions respectively. In plasmas, the y -axis is along the plasma density gradient and the x -axis is, of course, transverse to this direction. Also, keeping in mind our numerical simulations which will be described below, we introduced to the right-hand side (RHS) a hyperviscous dissipation of some degree $n \geq 2$ (a positive integer) and a small positive coefficient ν_n .

Introducing the Fourier transform of the streamfunction, $\psi_{\mathbf{k}} = \int \psi(\mathbf{x})e^{-i(\mathbf{k}\cdot\mathbf{x})} d\mathbf{x}$, the CHM equation, Eq. (1), ignoring the hyper-viscosity term for now, is equivalent to the following:

$$\begin{aligned} \partial_t \psi_{\mathbf{k}} &= +i\omega_{\mathbf{k}}\psi_{\mathbf{k}} \\ &+ \frac{1}{2} \sum_{\mathbf{k}_1, \mathbf{k}_2} T(\mathbf{k}, \mathbf{k}_1, \mathbf{k}_2) \psi_{\mathbf{k}_1} \psi_{\mathbf{k}_2} \delta(\mathbf{k} - \mathbf{k}_1 + \mathbf{k}_2), \end{aligned} \quad (3)$$

where

$$\omega_{\mathbf{k}} = -\frac{\beta k_x}{k^2 + F}, \quad (4)$$

$$T(\mathbf{k}, \mathbf{k}_1, \mathbf{k}_2) = -\frac{(\mathbf{k}_1 \times \mathbf{k}_2)_z (k_1^2 - k_2^2)}{k^2 + F} \quad (5)$$

and $\mathbf{k} = (k_x, k_y)$ and $k = |\mathbf{k}|$. The system clearly supports linear waves, known as Rossby or drift waves, in the GFD and plasma contexts respectively. They have the anisotropic dispersion relation given by Eq. (4). The structure of the nonlinear interaction, Eq. (5), is such

that the nonlinear term vanishes for a monochromatic wave. Hence Rossby waves are actually exact solutions of the full CHM equation. Much of this article will focus on the stability properties of these solutions.

Originally, the waves arise due to a primary instability, e.g. the baroclinic instability in GFD [28] or the ion-temperature-gradient instability (ITG) in fusion plasmas [31]. The instability is not included in the CHM equation, and it could be modeled by simulating CHM with an initial condition or introducing a linear forcing term on the RHS mimicking the linear instability (this would not take into account the nonlinear mechanisms in the wave forcing). It is interesting that the GFD-plasma analogy extends to the instabilities too in that the most unstable mode is "meridional" (i.e. along the x -axis) and concentrated at the scales of the order of ρ . Thus, in most of our considerations below we will consider the initial (primary) wave which is purely meridional.

SPECTRAL TRUNCATIONS

We shall use spectral truncations of Eq. (3) in our study of the stability properties of Rossby waves. They provide approximations of an intermediate degree of complexity between monochromatic waves and the full PDE. At this stage, such truncations should be viewed as ad-hoc since, in reality, all triads are coupled together in Eq. (3). Their usefulness will be determined by comparison with DNS solutions of the full system, Eq. (3). We shall consider two natural truncations: the 3-mode truncation and the 4-mode truncation.

3-Mode Truncation (3MT)

The simplest such truncation is to restrict the RHS of Eq. (3) to a single triad containing only 3 modes which we shall denote by \mathbf{p} , \mathbf{q} and $\mathbf{p}_- = \mathbf{p} - \mathbf{q}$. We construct the truncated equations by taking each wave vector in the triad in turn and assigning it to be \mathbf{k} in Eq. (3), enumerating all ways of assigning the others and their negatives to \mathbf{k}_1 and \mathbf{k}_2 on the RHS and neglect all terms which involve $\psi_{\mathbf{k}}$'s within the triad. Since $\psi_{\mathbf{k}}$ is the Fourier transform of a real field, $\psi_{-\mathbf{k}} = \bar{\psi}_{\mathbf{k}}$. We then arrive at the following equations for the 3-mode truncation:

$$\begin{aligned} \partial_t \psi_{\mathbf{p}} + i\omega_{\mathbf{p}} \psi_{\mathbf{p}} &= T(\mathbf{p}, \mathbf{q}, \mathbf{p}_-) \psi_{\mathbf{q}} \psi_{\mathbf{p}_-} \\ \partial_t \psi_{\mathbf{q}} + i\omega_{\mathbf{q}} \psi_{\mathbf{q}} &= T(\mathbf{q}, \mathbf{p}, -\mathbf{p}_-) \psi_{\mathbf{p}} \bar{\psi}_{\mathbf{p}_-} \\ \partial_t \psi_{\mathbf{p}_-} + i\omega_{\mathbf{p}_-} \psi_{\mathbf{p}_-} &= T(\mathbf{p}_-, \mathbf{p}, -\mathbf{q}) \psi_{\mathbf{p}} \bar{\psi}_{\mathbf{q}}. \end{aligned} \quad (6)$$

For most of what follows, it will be convenient to deal with Eqs. (6) in the interaction representation. Introduce $\Psi_{\mathbf{k}}(t) = \psi_{\mathbf{k}}(t)e^{-i\omega_{\mathbf{k}}t}$. In terms of $\Psi_{\mathbf{k}}$, Eqs. (6) become

$$\partial_t \Psi_{\mathbf{p}} = T(\mathbf{p}, \mathbf{q}, \mathbf{p}_-) \Psi_{\mathbf{q}} \Psi_{\mathbf{p}_-} e^{i\Delta_- t}$$

$$\begin{aligned} \partial_t \Psi_{\mathbf{q}} &= T(\mathbf{q}, \mathbf{p}, -\mathbf{p}_-) \Psi_{\mathbf{p}} \bar{\Psi}_{\mathbf{p}_-} e^{-i\Delta_- t} \\ \partial_t \Psi_{\mathbf{p}_-} &= T(\mathbf{p}_-, \mathbf{p}, -\mathbf{q}) \Psi_{\mathbf{p}} \bar{\Psi}_{\mathbf{q}} e^{-i\Delta_- t}, \end{aligned} \quad (7)$$

where

$$\Delta_- = \omega_{\mathbf{p}} - \omega_{\mathbf{q}} - \omega_{\mathbf{p}_-}.$$

A similar set of equations can be derived for the other natural triad, $(\mathbf{p}, -\mathbf{q}, \mathbf{p}_+)$ where $\mathbf{p}_+ = \mathbf{p} + \mathbf{q}$:

$$\begin{aligned} \partial_t \Psi_{\mathbf{p}} &= T(\mathbf{p}, -\mathbf{q}, \mathbf{p}_+) \bar{\Psi}_{\mathbf{q}} \Psi_{\mathbf{p}_+} e^{i\Delta_+ t} \\ \partial_t \Psi_{\mathbf{q}} &= T(\mathbf{q}, -\mathbf{p}, \mathbf{p}_+) \bar{\Psi}_{\mathbf{p}} \Psi_{\mathbf{p}_+} e^{i\Delta_+ t} \\ \partial_t \Psi_{\mathbf{p}_+} &= T(\mathbf{p}_+, \mathbf{p}, \mathbf{q}) \Psi_{\mathbf{p}} \Psi_{\mathbf{q}} e^{-i\Delta_+ t}, \end{aligned} \quad (8)$$

where

$$\Delta_+ = \omega_{\mathbf{p}} + \omega_{\mathbf{q}} - \omega_{\mathbf{p}_+}.$$

If $\Delta_{\pm} = 0$, the triad is exactly resonant. Then Eqs. (8) form an exactly integrable set of equations which have been extensively studied [32, 33].

4-Mode Truncation (4MT)

The 4MT model retains both triads, $(\mathbf{p}, \mathbf{q}, \mathbf{p}_+)$ and $(\mathbf{p}, -\mathbf{q}, \mathbf{p}_-)$, where $\mathbf{p}_{\pm} = \mathbf{p} \pm \mathbf{q}$ mentioned above. A thorough analysis of the 4-mode truncation for the Generalised Hasegawa-Mima equation in the case of weak nonlinearity was presented in [34]. The truncated equations combine Eqs. (7) and Eqs. (8):

$$\begin{aligned} \partial_t \Psi_{\mathbf{p}} &= T(\mathbf{p}, \mathbf{q}, \mathbf{p}_-) \Psi_{\mathbf{q}} \Psi_{\mathbf{p}_-} e^{i\Delta_- t} \\ &\quad + T(\mathbf{p}, -\mathbf{q}, \mathbf{p}_+) \bar{\Psi}_{\mathbf{q}} \Psi_{\mathbf{p}_+} e^{i\Delta_+ t} \\ \partial_t \Psi_{\mathbf{q}} &= T(\mathbf{q}, \mathbf{p}, -\mathbf{p}_-) \Psi_{\mathbf{p}} \bar{\Psi}_{\mathbf{p}_-} e^{-i\Delta_- t} \\ &\quad + T(\mathbf{q}, -\mathbf{p}, \mathbf{p}_+) \bar{\Psi}_{\mathbf{p}} \Psi_{\mathbf{p}_+} e^{i\Delta_+ t} \\ \partial_t \Psi_{\mathbf{p}_-} &= T(\mathbf{p}_-, \mathbf{p}, -\mathbf{q}) \Psi_{\mathbf{p}} \bar{\Psi}_{\mathbf{q}} e^{-i\Delta_- t} \\ \partial_t \Psi_{\mathbf{p}_+} &= T(\mathbf{p}_+, \mathbf{p}, \mathbf{q}) \Psi_{\mathbf{p}} \Psi_{\mathbf{q}} e^{-i\Delta_+ t}. \end{aligned} \quad (9)$$

Strictly speaking, the chosen four modes ($\psi_0, \psi_{\mathbf{q}}, \psi_+$ and ψ_-) are coupled to further modes and do not form a closed system. Indeed, even the linear problem closes only if all the satellites $\pm\mathbf{q} + m\mathbf{p}$ (m is a positive or negative integer) are included [1]. However, in considering the linear instability it is traditional to truncate the system to the four modes only with a justification that the higher order satellites are less excited in the linear eigenvectors, which turns out to be a very good approximation if $M \ll 1$ and quite reasonable for $M \sim 1$ and larger [1]. In this paper we will test predictions of the 4MT system, both linear and nonlinear, against DNS of the full system.

Nonlinearity parameter M

In studying instability of a primary monochromatic wave, we will follow the convention that the wavenumber of this wave is \mathbf{p} and denoted its amplitude by $\Psi_{\mathbf{p}}$. The character of the instability is greatly influenced by the initial amplitude of the primary wave, $\Psi_0 = \Psi_{\mathbf{p}}|_{t=0}$ [1]. Following Gill [1], we introduce the nonlinearity parameter

$$M = \frac{\Psi_0 p^3}{\beta}. \quad (10)$$

M measures the relative strength of the linear and non-linear terms at the scale of the carrier wave. $M \gg 1$ corresponds to the case where the β -effect plays no role. For $F = 0$ this case reduces to the Euler equation limit and the well-studied instability of the plane parallel sinusoidal shear flow known as Kolmogorov flow [26]. Note that most papers on the modulational instability within the plasma context have dealt only with this limit (e.g. [20, 21]). Case $M \ll 1$ corresponds to the weak non-linearity limit dominated by resonant wave triads. In this case the four constituent modes (carrier wave, modulation and two satellites) can be split into two coupled triads which produce independent contributions to the instability [1]. The instability associated with a single triad is known as the decay instability [27]. The condition $M \sim 1$ defines the Rhines scale k_r , which marks a crossover from the hydrodynamic vortex to the wave behavior [35].

DECAY INSTABILITY OF A ROSSBY WAVE

The decay instability is an instability of a carrier wave involving a pair of other modes (i.e. the primary wave decays into two secondary waves, see e.g. [27]). We shall derive this instability from the 3MT, Eqs. (7). Introducing the vector notation $\Psi = (\Psi_{\mathbf{p}}, \Psi_{\mathbf{q}}, \Psi_{\mathbf{p}_-})$, a monochromatic carrier wave is given by $\Psi_0 = (\Psi_0, 0, 0)$ where Ψ_0 is a complex constant representing the amplitude of the initial carrier wave. This is an exact solution of Eqs. (7). We consider the stability of this solution to small perturbations involving the modes \mathbf{q} and \mathbf{p}_- by taking $\Psi = \Psi_0 + \epsilon \Psi_1$ with the perturbation given by $\Psi_1 = (0, \tilde{\psi}_{\mathbf{q}}, \tilde{\psi}_{\mathbf{p}_-})$. Linearisation yields the following equations at first order in ϵ :

$$\begin{aligned} \partial_t \tilde{\psi}_{\mathbf{q}} &= T(\mathbf{q}, \mathbf{p}, -\mathbf{p}_-) \Psi_0 \tilde{\psi}_{\mathbf{p}_-} e^{-i\Delta_- t} \\ \partial_t \tilde{\psi}_{\mathbf{p}_-} &= T(\mathbf{p}_-, \mathbf{p}, -\mathbf{q}) \bar{\Psi}_0 \tilde{\psi}_{\mathbf{q}} e^{i\Delta_- t}. \end{aligned} \quad (11)$$

We now seek harmonic solutions:

$$\begin{aligned} \tilde{\psi}_{\mathbf{q}}(t) &= A_{\mathbf{q}} e^{-i\Omega_{\mathbf{q}} t} \\ \tilde{\psi}_{\mathbf{p}_-}(t) &= A_{\mathbf{p}_-} e^{-i\Omega_{\mathbf{p}_-} t}. \end{aligned}$$

This requires $\bar{\Omega}_{\mathbf{p}_-} = -\Omega_{\mathbf{q}} + \Delta_-$. Solving Eqs. (11) then reduces to finding solutions of the linear system

$$A \begin{pmatrix} A_{\mathbf{q}} \\ \bar{A}_{\mathbf{p}_-} \end{pmatrix} = 0$$

where

$$A = \begin{pmatrix} -i\Omega_{\mathbf{q}} & T(\mathbf{q}, \mathbf{p}, -\mathbf{p}_-) \Psi_0 \\ T(\mathbf{p}_-, \mathbf{p}, -\mathbf{q}) \bar{\Psi}_0 & i(-\Omega_{\mathbf{q}} + \Delta_-) \end{pmatrix} \quad (12)$$

To obtain non-trivial solutions, we require $\det A = 0$, which yields the dispersion relation:

$$\Omega_{\mathbf{q}}(-\Omega_{\mathbf{q}} + \Delta_-) - T(\mathbf{q}, \mathbf{p}, -\mathbf{p}_-) T(\mathbf{p}_-, \mathbf{p}, -\mathbf{q}) |\Psi_0|^2 = 0. \quad (13)$$

This has two roots, $\Omega_{\mathbf{q}}^{\pm}$ with corresponding eigenvectors:

$$\begin{pmatrix} A_{\mathbf{q}} \\ \bar{A}_{\mathbf{p}_-} \end{pmatrix} = \begin{pmatrix} 1 \\ \frac{T(\mathbf{p}_-, \mathbf{p}, -\mathbf{q}) \Psi_0}{i(\Omega_{\mathbf{q}} - \Delta_-)} \end{pmatrix}. \quad (14)$$

Instability occurs when $\Omega_{\mathbf{q}}$ has a non-zero imaginary part. For an exactly resonant triad, $\Delta_- = 0$. For resonant triads, using Eq. (5) the roots of Eq. (13) are

$$\Omega_{\mathbf{q}} = \pm i \frac{|\Psi_0| |\mathbf{p} \times \mathbf{q}|}{\sqrt{(q^2 + F)(p_-^2 + F)}} \sqrt{(p^2 - q^2)(p_-^2 - p^2)}. \quad (15)$$

In this case, instability occurs if $q < p < p_-$.

Before investigating the non-resonant instability further, it is convenient to perform some rescalings. The dimensionless carrier wave amplitude will be given by M defined in Eq. (10). We non-dimensionalise the other terms in Eq. (13) as follows:

$$\begin{aligned} \Omega &\rightarrow \frac{\beta}{p} \Omega, \\ F &\rightarrow p^2 F, \\ \mathbf{p} &\rightarrow p \hat{\mathbf{p}}, \\ \mathbf{q} &\rightarrow sp \hat{\mathbf{q}}, \end{aligned}$$

where $\hat{\mathbf{p}} = (\hat{p}_x, \hat{p}_y)$ and $\hat{\mathbf{q}} = (\hat{q}_x, \hat{q}_y)$ are unit vectors pointing in the directions of \mathbf{p} and \mathbf{q} respectively. Eq. (13) can then be re-arranged to the following form:

$$\Omega(-\Omega + \hat{\Delta}_-) - M^2 T(s\hat{\mathbf{q}}, \hat{\mathbf{p}}, -\hat{\mathbf{p}}_-) T(\hat{\mathbf{p}}_-, \hat{\mathbf{p}}, -\hat{\mathbf{q}}) = 0. \quad (16)$$

where $\hat{\mathbf{p}}_- = \hat{\mathbf{p}} - s\hat{\mathbf{q}}$ and $\hat{\Delta}_- = \omega_{\hat{\mathbf{p}}} - \omega_{s\hat{\mathbf{q}}} - \omega_{\hat{\mathbf{p}}_-}$. The two roots are

$$\Omega_{\pm} = \frac{1}{2} \left(\hat{\Delta}_- \pm \sqrt{(\hat{\Delta}_-)^2 - 4M^2 T(s\hat{\mathbf{q}}, \hat{\mathbf{p}}, -\hat{\mathbf{p}}_-) T(\hat{\mathbf{p}}_-, \hat{\mathbf{p}}, -\hat{\mathbf{q}})} \right) \quad (17)$$

To have an instability we require

$$\hat{\Delta}_- < 2M \sqrt{T(s\hat{\mathbf{q}}, \hat{\mathbf{p}}, -\hat{\mathbf{p}}_-) T(\hat{\mathbf{p}}_-, \hat{\mathbf{p}}, -\hat{\mathbf{q}})}$$

which demonstrates that the instability concentrates on the resonant manifold, $\hat{\Delta}_- = 0$ as $M \rightarrow 0$. This is illustrated in Fig. 1. The corresponding analysis for the triad

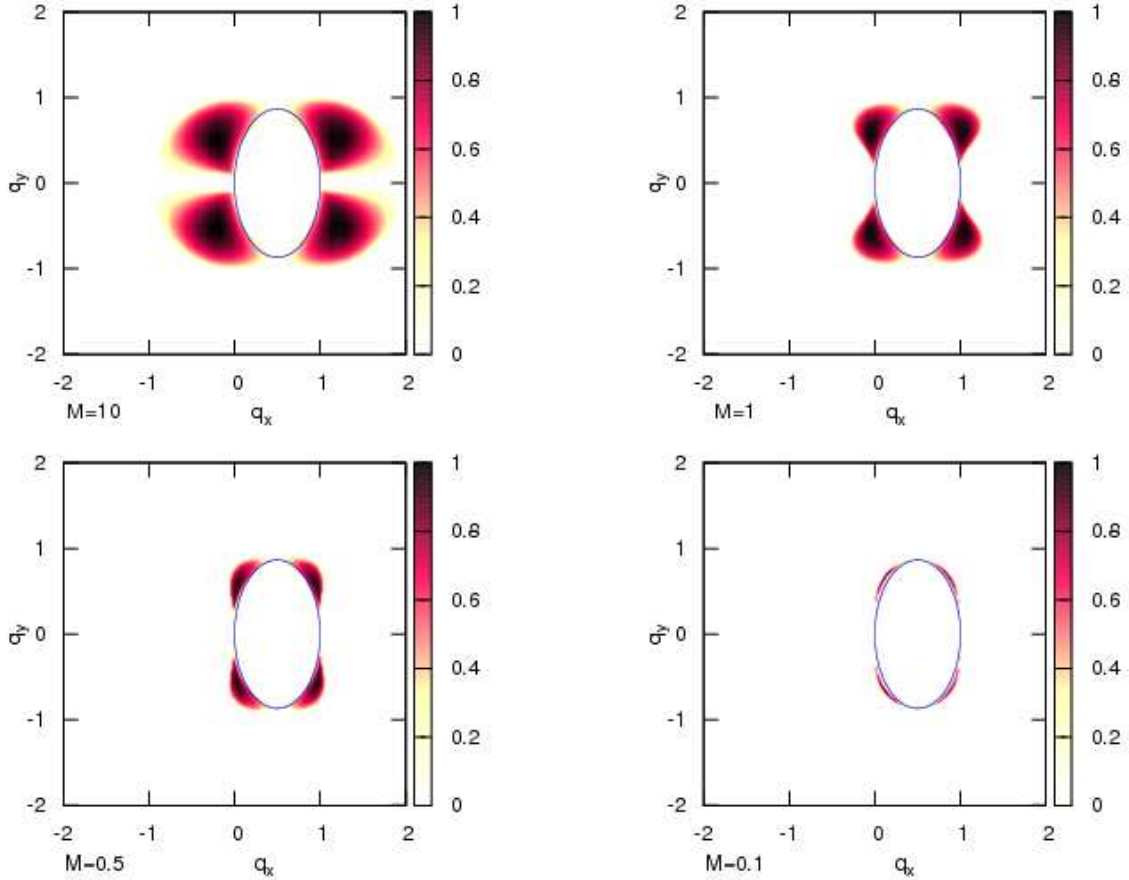


FIG. 1: The growth rate of the decay instability (the negative imaginary part of the roots of Eq.(16)) is plotted as a function of \mathbf{q} for a fixed meridional carrier wave-vector, $\hat{\mathbf{p}} = (1, 0)$, for various values of the nonlinearity parameter M . The set of unstable perturbations become concentrated on the resonant manifolds (blue lines) as the nonlinearity of the carrier wave is decreased.

$(\mathbf{p}, -\mathbf{q}, \mathbf{p}_+)$ produces identical surfaces reflected about the vertical axis reflecting the instability concentrating on the second resonant manifold, $\hat{\Delta}_+ = 0$. As $M \rightarrow 0$, these two surfaces become disjoint from each other except near the origin $\mathbf{q} = 0$.

MODULATIONAL INSTABILITY: LINEAR ANALYSIS

Let us now derive the modulational instability in the same way as we have done for the decay instability. The modulational instability is studied using the 4MT. We begin by linearising Eqs. (9) about the pure carrier wave solution, $\Psi_0 = (\Psi_0, 0, 0, 0)$ where Ψ_0 is a complex constant representing the amplitude of the initial carrier wave. We consider the stability of this solution to small

perturbations involving the 3 modes \mathbf{q} , \mathbf{p}_- and \mathbf{p}_+ by taking $\Psi = \Psi_0 + \epsilon\Psi_1$ with the perturbation given by $\Psi_1 = (0, \tilde{\psi}_{\mathbf{q}}, \tilde{\psi}_{\mathbf{p}_+}, \tilde{\psi}_{\mathbf{p}_-})$. Linearisation yields the following equations at first order in ϵ :

$$\begin{aligned} \partial_t \tilde{\psi}_{\mathbf{q}} &= T(\mathbf{q}, \mathbf{p}, -\mathbf{p}_-) \Psi_0 \tilde{\psi}_{\mathbf{p}_-} e^{-i\Delta_- t} \\ &\quad + T(\mathbf{q}, -\mathbf{p}, \mathbf{p}_+) \bar{\Psi}_0 \tilde{\psi}_{\mathbf{p}_+} e^{i\Delta_+ t} \\ \partial_t \tilde{\psi}_{\mathbf{p}_+} &= T(\mathbf{p}_+, \mathbf{p}, \mathbf{q}) \Psi_0 \tilde{\psi}_{\mathbf{q}} e^{-i\Delta_+ t} \\ \partial_t \tilde{\psi}_{\mathbf{p}_-} &= T(\mathbf{p}_-, \mathbf{p}, -\mathbf{q}) \bar{\Psi}_0 \tilde{\psi}_{\mathbf{q}} e^{i\Delta_- t}. \end{aligned} \quad (18)$$

We again seek harmonic solutions:

$$\begin{aligned} \tilde{\psi}_{\mathbf{q}}(t) &= A_{\mathbf{q}} e^{-i\Omega_{\mathbf{q}} t} \\ \tilde{\psi}_{\mathbf{p}_+}(t) &= A_{\mathbf{p}_+} e^{-i\Omega_{\mathbf{p}_+} t} \\ \tilde{\psi}_{\mathbf{p}_-}(t) &= A_{\mathbf{p}_-} e^{-i\Omega_{\mathbf{p}_-} t}. \end{aligned}$$

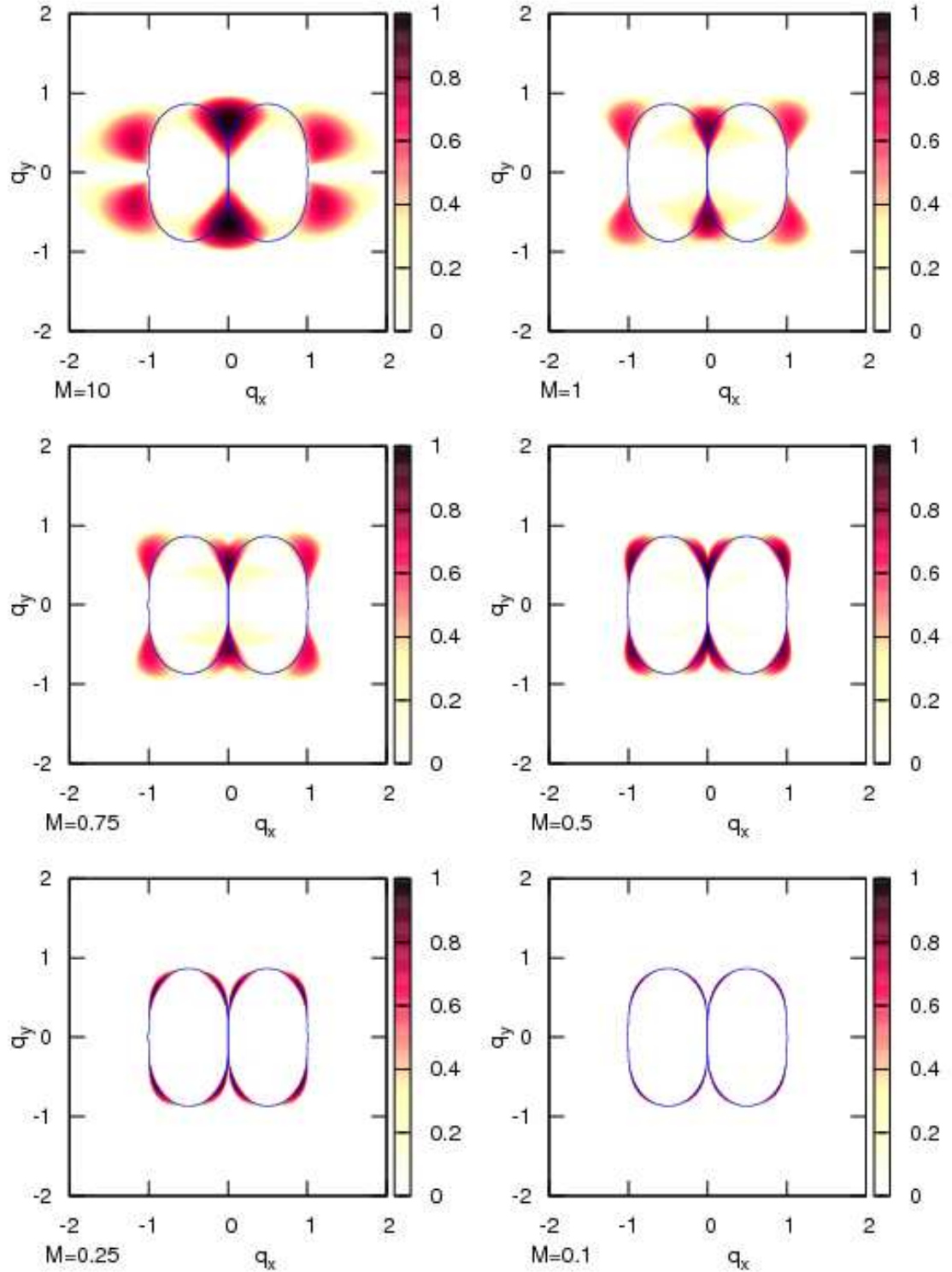


FIG. 2: Growth rate of the modulational instability (the negative imaginary part of the roots of Eq.(23)) as a function of \mathbf{q} for a fixed meridional carrier wave-vector, $\mathbf{p} = (1, 0)$ and $F = 0$. The values of the nonlinearity M for the initial carrier wave are $M = 10$ (Euler limit), $M = 1$, $M = 3/4$, $M = 1/2$, $M = 1/4$ and $M = 1/10$ (weakly nonlinear limit). The set of unstable perturbations become concentrated on the resonant manifolds as the nonlinearity of the carrier wave is decreased.

This requires requires $\Omega_{\mathbf{p}_+} = \Omega_{\mathbf{q}} + \Delta_+$ and $\bar{\Omega}_{\mathbf{p}_-} = -\Omega_{\mathbf{q}} + \Delta_-$. Solving Eqs. (18) then reduces to finding solutions of the linear system

$$A \begin{pmatrix} A_{\mathbf{q}} \\ A_{\mathbf{p}_+} \\ A_{\mathbf{p}_-} \end{pmatrix} = 0$$

where

$$A = \begin{pmatrix} i\Omega_{\mathbf{q}} & T(\mathbf{q}, -\mathbf{p}, \mathbf{p}_+) \bar{\Psi}_0 & T(\mathbf{q}, \mathbf{p}, -\mathbf{p}_-) \Psi_0 \\ T(\mathbf{p}_+, \mathbf{p}, \mathbf{q}) \Psi_0 & i(\Omega_{\mathbf{q}} + \Delta_+) & 0 \\ T(\mathbf{p}_-, \mathbf{p}, -\mathbf{q}) \bar{\Psi}_0 & 0 & -i(-\Omega_{\mathbf{q}} + \Delta_-) \end{pmatrix} \quad (19)$$

Setting $\det A = 0$ yields a cubic dispersion relation:

$$\Omega_{\mathbf{q}}(\Omega_{\mathbf{q}} + \Delta_+)(-\Omega_{\mathbf{q}} + \Delta_-) \quad (20)$$

$$+T(\mathbf{q}, -\mathbf{p}, \mathbf{p}_+) T(\mathbf{p}_+, \mathbf{p}, \mathbf{q}) |\Psi_0|^2 (-\Omega_{\mathbf{q}} + \Delta_-) \\ -T(\mathbf{q}, \mathbf{p}, -\mathbf{p}_-) T(\mathbf{p}_-, \mathbf{p}, -\mathbf{q}) |\Psi_0|^2 (\Omega_{\mathbf{q}} + \Delta_+) = 0.$$

The corresponding eigenvectors are given by

$$\begin{pmatrix} A_{\mathbf{q}} \\ A_{\mathbf{p}_+} \\ A_{\mathbf{p}_-} \end{pmatrix} = \begin{pmatrix} 1 \\ \frac{T(\mathbf{p}_+, \mathbf{p}, \mathbf{q}) \Psi_0}{-i(\Omega_{\mathbf{q}} + \Delta_+)} \\ \frac{T(\mathbf{p}_-, \mathbf{p}, -\mathbf{q}) \bar{\Psi}_0}{i(\Omega_{\mathbf{q}} - \Delta_-)} \end{pmatrix}. \quad (21)$$

This derivation holds for any system with a quadratic nonlinearity. Using Eq. (5) and performing some algebra we recover the usual form of the dispersion relation specific to the CHM equation [1] (see also [2, 18, 20, 21]):

$$(q^2 + F)\Omega + \beta q_x + |\Psi_0|^2 |\mathbf{p} \times \mathbf{q}|^2 (p^2 - q^2) \left[\frac{p_+^2 - p^2}{(p_+^2 + F)(\Omega + \omega) + \beta p_{+x}} - \frac{p_-^2 - p^2}{(p_-^2 + F)(\Omega - \omega) + \beta p_{-x}} \right] = 0 \quad (22)$$

This can be solved numerically, and sometimes analytically, for a given set of parameters to determine Ω . For the purposes of easy comparison of different values of M , we nondimensionalise as before. The result is

$$(s^2 + F)\Omega + s\hat{q}_x + M^2 s^2 (1 - s^2) |\hat{\mathbf{p}} \times \hat{\mathbf{q}}|^2 [T^+ - T^-] = 0, \quad (23)$$

where

$$T^\pm = \frac{|\hat{\mathbf{p}} \pm s\hat{\mathbf{q}}|^2 - 1}{(|\hat{\mathbf{p}} \pm s\hat{\mathbf{q}}| + F) \left(-\frac{\hat{p}_x}{1+F} \pm \Omega \right) + \hat{p}_x \pm s\hat{q}_x}. \quad (24)$$

The roots of this equation are controlled by five parameters, M , F , s , θ_p and θ_q where θ_p and θ_q are the angles between the x-axis and the carrier wave-vector and perturbation wave-vector respectively. The structure of the instability is strongly dependent on the value of M . This is shown in Fig. 2. We see that the modulational instability is, in some sense, the nonlinear sum of the decay instabilities for the two triads, and we will clarify this issue in the next section.

COMPARISON OF THE 3MT AND THE 4MT MODELS WITH DNS OF THE FULL CHM SYSTEM

There is sometimes confusion in the literature, perhaps partially semantic, on whether the modulational instability of the Rossby and drift waves is governed by 3-wave or 4-wave interactions. Here we will clarify this issue. It was shown by Gill [1] that as $M \rightarrow 0$, the modulational

instability obtained within the 4MT model localises on the two resonant manifolds for the two triads $\Delta_+ = 0$ and $\Delta_- = 0$. Since these two curves are mostly disjoint from each other (except for the origin), in the weakly nonlinear limit, the modulational instability is just a simple sum of the two decay instabilities. Namely, the two unstable eigenvectors of the instability of the 4MT will coincide with the eigenvectors of the two respective branches of the decay instability (i.e. the fourth mode in such 4MT eigenvectors will have zero amplitude). In particular, the maximum growth rates of the 3MT and 4MT instabilities become identical. For larger values of M , the growth rate of the modulational instability is typically larger than that of the corresponding decay instability.

However, for the typical setup where the primary wave is purely meridional and the modulation is purely zonal, the wavevector \mathbf{q} is equally close to both branches of the three-wave resonant manifold. This is because these resonant manifolds cross zero of the \mathbf{q} -space in the direction of the q_y -axis, i.e. in the zonal direction. Thus, the above speculations about the equivalence of the 3MT and the 4MT for weak waves may not apply to such a setup. Therefore, let us consider the weakly nonlinear case ($M = 0.1$) and examine predictions of the 3MT and the 4MT models and compare them to DNS of the full CHM system in the following two cases:

- (A) the primary wave is purely meridional, $\mathbf{p} = (10, 0)$, and the modulation is purely zonal, $\mathbf{q} = (0, 1)$; and
- (B) the primary wave is purely meridional, $\mathbf{p} = (10, 0)$, and the modulation is off-zonal. We take $\mathbf{q} = (9, 6)$.

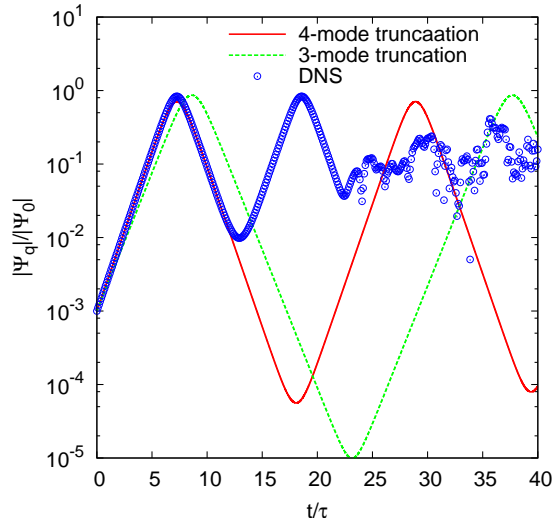


FIG. 3: Amplitude of the zonal mode with wavenumber \mathbf{q} for $M = 0.1$, $\mathbf{p} = (10, 0)$ obtained from DNS and from solutions of 3MT and 4MT models. Case (i): purely zonal modulations, $\mathbf{q} = (0, 1)$.

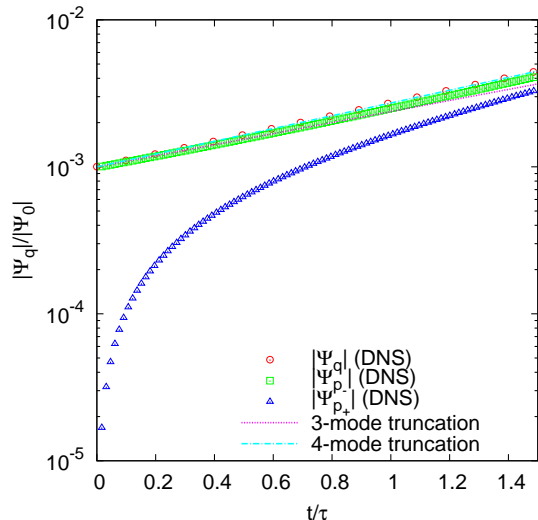


FIG. 4: Comparison of modulatory and decay instabilities for early times for the case (i) -purely zonal modulations (like in Fig. 3).

This is close to the maximum of the most unstable mode on the resonant curve. We cannot select the exact value of the maximum because the discrete wave numbers in the periodic box do not typically lie exactly on the resonant manifolds. This is a subtlety which can have strong implications for numerical simulations of very weakly nonlinear regimes [36] which we have been careful to avoid here.

Let us first consider case (A) when the modulation is purely zonal. Fig. 3 compares $|\Psi_{\mathbf{q}}|$ obtained from the solution of Eq. (3) with that obtained from solutions of 3MT, Eqs. (7), and 4MT, Eqs. (9). The initial condition

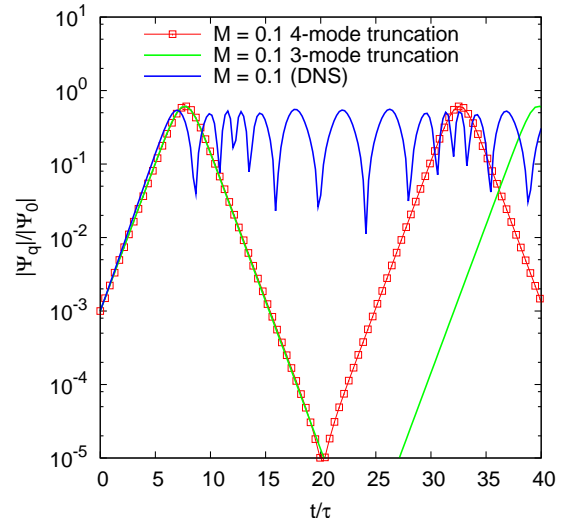


FIG. 5: Same as in Fig. 3 but now for the case (ii): off-zonal modulations, $\mathbf{q} = (9, 6)$.

was constructed from Eq. (14), the unstable eigenvector for the decay instability. We see that the growth rate predicted for the decay instability is not observed. The PDE instead seems to follow the growth rate for the modulational instability. From the zoomed-in plot of the early time evolution shown in Fig. 4 we see that the full dynamics very quickly generates the mode \mathbf{p}_+ which is absent from Eqs. (6). The full system then quickly deviates from the solution of the 3MT in a time of the order of the inverse of the instability growth rate. However, the set of 4 modes takes much longer to generate any further modes. Thus in this setup, the 4MT Eqs. (9) provide a much better description of the full dynamics for times up to 10 instability times.

Let us now consider the case (B) when the modulation is off-zonal. Fig. 5 compares $|\Psi_{\mathbf{q}}|$ obtained from the solution of Eq. (3) with that obtained from solutions of 3MT, Eqs. (7), and 4MT, Eqs. (9), for an initial condition being the unstable eigenvector for the decay instability, Eq. (14). As expected, now the 3MT and the 4MT give practically identical results, and both of these models agree well with DNS up to the time equal to seven inverse growth rates. They predict well the maximum of the zonal jet amplitude, although the subsequent stage of decrease is not described as well as in case (A) by the 4MT model.

From these results we conclude that the 3-wave interaction is indeed the basic nonlinear process when $M \ll 1$ provided the triad is not degenerate, in the sense that it does not contain quasi-resonant modes which are equidistant from two different resonant manifolds as happens when the vector \mathbf{q} is zonal. In these cases, the 3MT system is just as good as the 4MT and it describes well the full CHM system for over several characteristic times (i.e. the inverse instability growth rates). On the other

hand, the most relevant configuration with \mathbf{q} zonal is, in fact, degenerate. In this case, however, the 4MT model works well over many characteristic times whereas the 3MT fails almost immediately. Thus, to have a wider range of applicability, we will study the 4MT model and abandon the 3MT model in the remainder of the present paper.

Next, let us study the modulational instability arising from the 4MT in greater detail.

INSTABILITY FOR PURELY MERIDIONAL CARRIER WAVE AND PURELY ZONAL MODULATION

The case of a purely zonal carrier wave ($\hat{\mathbf{p}} = (1, 0)$) and purely meridional perturbation ($\hat{\mathbf{q}} = (0, 1)$) is of physical interest and produces considerable simplification. The dispersion relation then reduces to solving

$$\Omega^3 + \left(\frac{s^2}{(1+F)(s^2+1+F)} \right)^2 \left(\frac{2M^2(1-s^2)(1+F)^2(s^2+F+1) - (s^2+F)}{s^2+F} \right) \Omega = 0, \quad (25)$$

which has roots

$$\Omega = 0 \quad (26)$$

$$\Omega = \pm i \left(\frac{s^2}{(1+F)(s^2+1+F)} \right) \sqrt{\frac{2M^2(1-s^2)(1+F)^2(s^2+F+1) - (s^2+F)}{s^2+F}} \quad (27)$$

The question of whether the perturbation is unstable reduces to the question of when the quantity under the square root is positive. In this expression, recall that s is the ratio, q/p , of the modulus of the modulation wave-vector to the modulus of the primary wave-vector. Letting $s^2 = y$, one obtains a quadratic for the quantity under the square root which is positive in the range $s \in (-s_{\max}, s_{\max})$ where

$$s_{\max}^2 = \frac{1 + 2M^2F(1+F)^2}{2M^2(1+F)^2} \left[-1 + \sqrt{1 + 4 \frac{(2M^2(1+F)^3 - F)(2M^2(1+F)^2)}{(1 + 2M^2F(1+F)^2)^2}} \right] \quad (28)$$

Case of Infinite Deformation Radius

When $F = 0$ the analysis becomes particularly simple. There is always a range of unstable long wavelength perturbations, given by $(0, s_{\max})$, for any value of M . s_{\max} is given by

$$s_{\max} = \sqrt{\frac{-1 + \sqrt{1 + 16M^4}}{4M^2}}. \quad (29)$$

Within this range the growth rate is

$$\Omega = \left(\frac{s^2}{(s^2+1)} \right) \sqrt{2M^2(1-s^4) - s^2}. \quad (30)$$

The growth rate has a single maximum at $s_0 = \sqrt{y_0}$ where y_0 is the positive root of

$$y^3 + 3y^2 + \left(1 + \frac{1}{M^2}\right)y - 1 = 0. \quad (31)$$

One can show that $s_0 \rightarrow \sqrt{\sqrt{2}-1}$ as $M \rightarrow \infty$ and $s_0 = M + O(M^2)$ as $M \rightarrow 0$. One would be interested to know when the maximally unstable meridional perturbation is a local maximum with respect to nearby non-meridional

perturbations. To ascertain this, one should look at the sign of the determinant

$$\Delta_M(\hat{q}_x, \hat{q}_y) = \begin{vmatrix} \frac{\partial^2 \Omega}{\partial^2 \hat{q}_x} & \frac{\partial^2 \Omega}{\partial \hat{q}_x \partial \hat{q}_y} \\ \frac{\partial^2 \Omega}{\partial \hat{q}_x \partial \hat{q}_y} & \frac{\partial^2 \Omega}{\partial^2 \hat{q}_y} \end{vmatrix} \quad (32)$$

evaluated at $(\hat{q}_x, \hat{q}_y) = (0, s_0)$. This can be done semi-analytically using *Mathematica* and is plotted in the inset of Fig. 6. We find that $\Delta_M > 0$ with $\frac{\partial^2 \Omega}{\partial^2 \hat{q}_x} < 0$ (the criterion for a local maximum) for $M > M_c$. $\Delta_M < 0$ with $\frac{\partial^2 \Omega}{\partial^2 \hat{q}_x} < 0$ (the criterion for a saddle) for $M < M_c$. The critical value of M is found numerically to be $M_c \approx 0.534734$. Numerical explorations show that the local maximum found for $M > M_c$, is actually global. For $M > M_c$, therefore, the fastest growing perturbation is indeed zonal. As M decreases below M_c the most unstable perturbation moves to a point with a finite value of q_x . The maximally unstable perturbation for $M < 0.53$ tends to a point on the resonant manifold making an angle of $5\pi/6$ with the x -axis. The dependence of this angle on M is shown in Fig. 6. A clear transition from an axial maximum to an off-axis maximum is clearly visible.

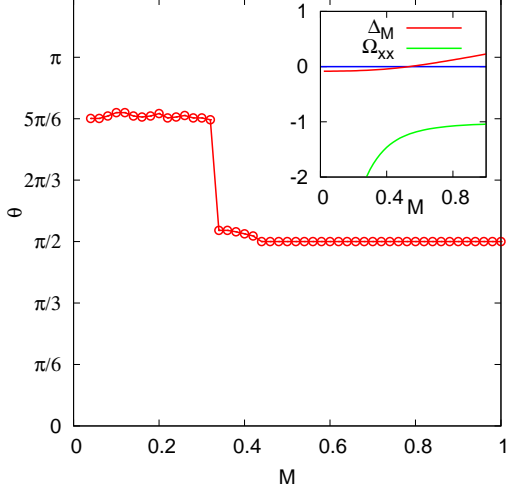


FIG. 6: Angle, θ , between the \mathbf{q} wave-vector of the maximally unstable perturbation and the x -axis as a function of M . Inset plots Δ_M and Ω_{xx} as a function of M illustrating the transition of the maximum growth rate for on-axis perturbations from a local maximum to a saddle point at $M \approx 0.53$.

Effects of Finite Deformation Radius

We now consider the dependence of MI on the deformation or Larmor radius, noting that a finite deformation radius is obtained in the QG system under a reduced gravity approximation. When F is finite, there are 2 regimes, depending on the value of M . For an interval of instability to exist, we require $s_{\max}^2 > 0$. This requires that

$$p(F) = 2M^2(1 + F)^3 - F > 0. \quad (33)$$

The discriminant of the corresponding cubic, $p(F) = 0$, is $-4(-2M^2 + 27M^4)$. Since we are only interested in $F > 0$ we can identify two regimes.

- Regime 1: $M > \sqrt{\frac{2}{27}}$

Referring to Eq. (28), $p(F) = 0$ has one real root, F_1 (which is negative) and $p(F) > 0$ when $F > F_1$. Then for any positive value of F there exists a finite range of s , $s \in (0, s_{\max})$, for which the perturbation is unstable. s_{\max} is given by Eq. (28). In this regime, finite deformation radius tends to reduce the growth rate of the instability but cannot suppress it. See Fig. 7.

- Regime 2: $M \leq \sqrt{\frac{2}{27}}$

Referring to Eq. (28), $p(F) = 0$ has three real roots, F_1 , F_2 and F_3 . F_1 is negative and F_2 and F_3 are positive. $p(F) < 0$ in the range (F_2, F_3) . In this regime, there are critical values of F , F_1 and F_2 such that the range $s \in (0, s_{\max})$ of unstable perturbations only exists if $F < F_1$ or $F > F_2$. F_1 and F_2

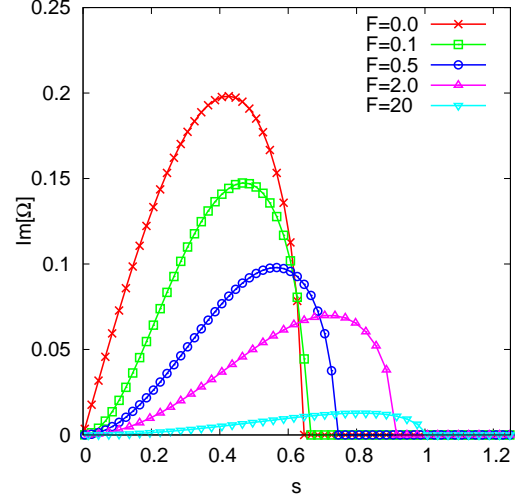


FIG. 7: Instability growthrate for purely meridional perturbations with $M = 0.5 > \sqrt{2/27}$ for different values of the deformation radius.

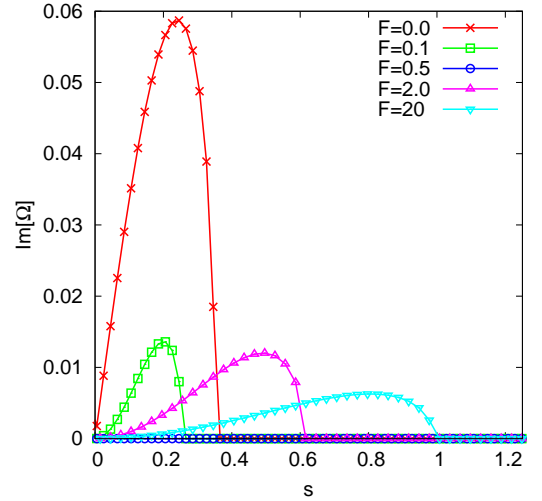


FIG. 8: Instability growthrate for purely meridional perturbations with $M = 0.25 < \sqrt{2/27}$ for different values of the deformation radius. For this value of M , $F_2 \approx 0.23$ and $F_3 \approx 1.00$. Note that the instability is completely suppressed for intermediate values of F and then emerges again as F increases.

are obtained by finding the positive roots of Eq. 33 and s_{\max} is again given by Eq. (28). In this regime, there is a range of intermediate deformation radii which completely suppresses the instability. See Fig. 8.

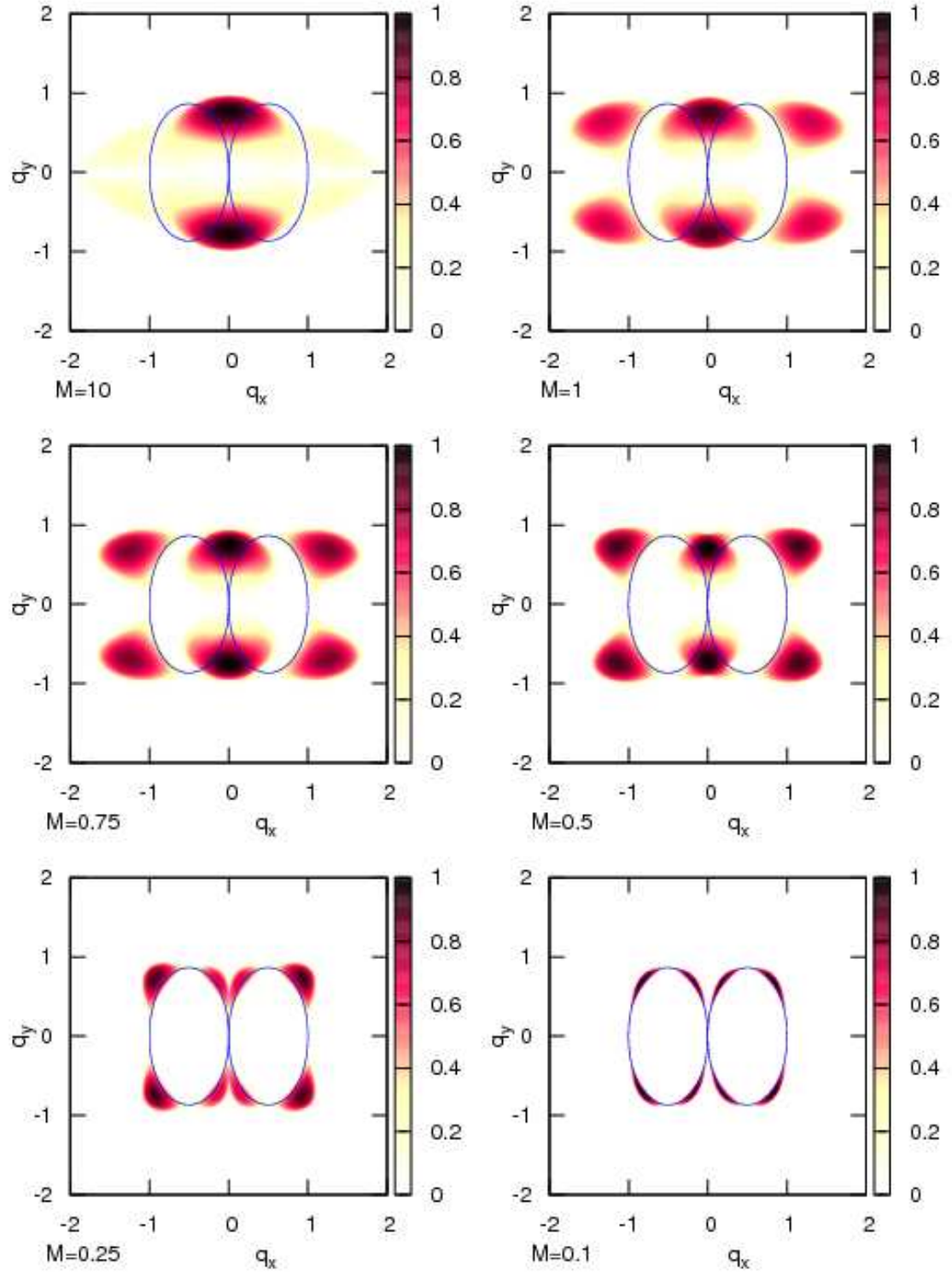


FIG. 9: Same as in Fig. 2 but now for a finite deformation radius, $F = 2$.

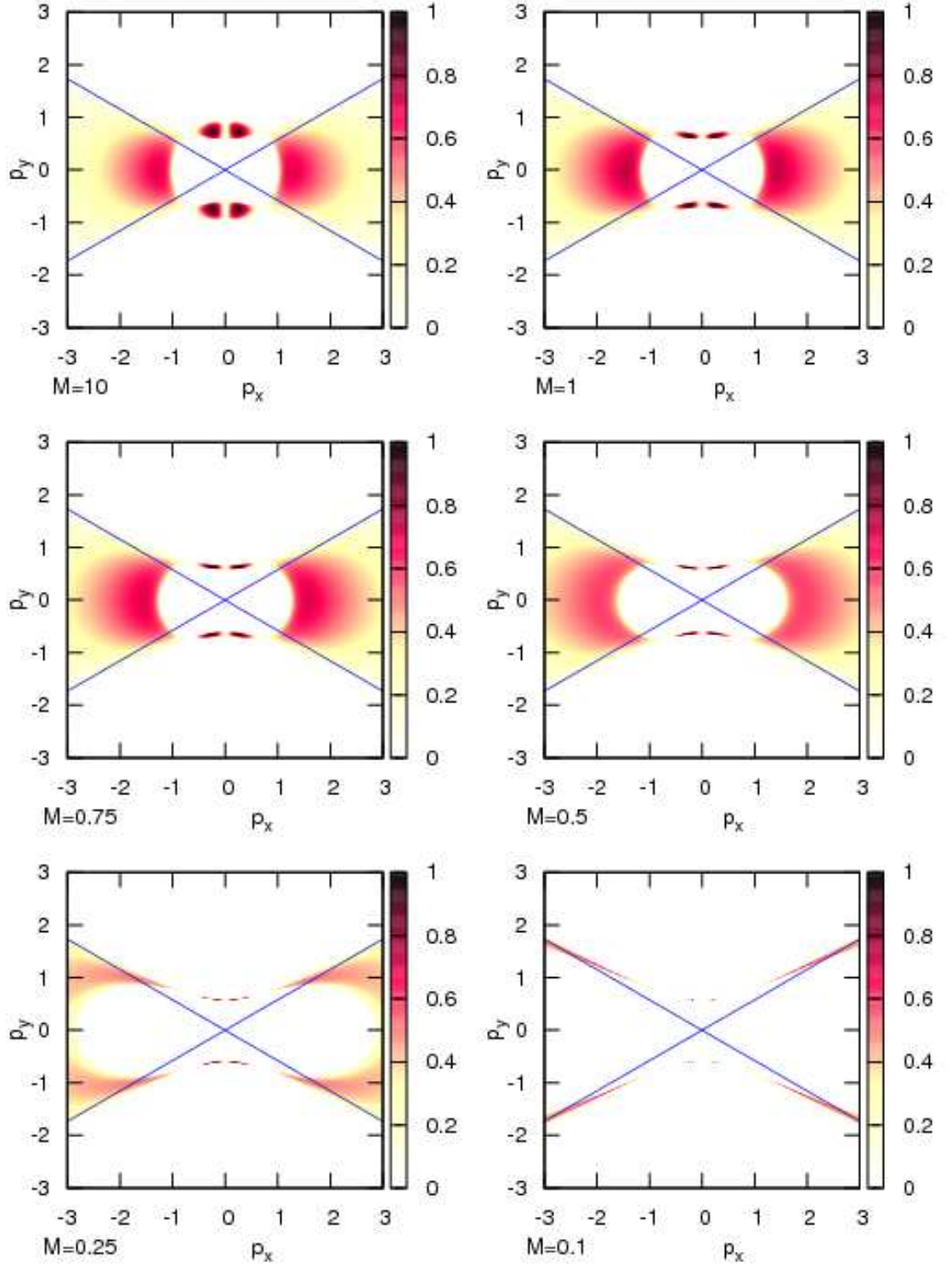


FIG. 10: Growth rate of the modulational instability (found from Eq.(23)) as a function of \mathbf{p} for a fixed zonal modulation wave-vector, $\mathbf{q} = (0, 1)$ and $F = 0$. The values of M for the initial carrier wave are $M = 10$ (Euler limit), $M = 1$, $M = 3/4$, $M = 1/2$, $M = 1/4$ and $M = 1/10$ (weakly nonlinear limit).

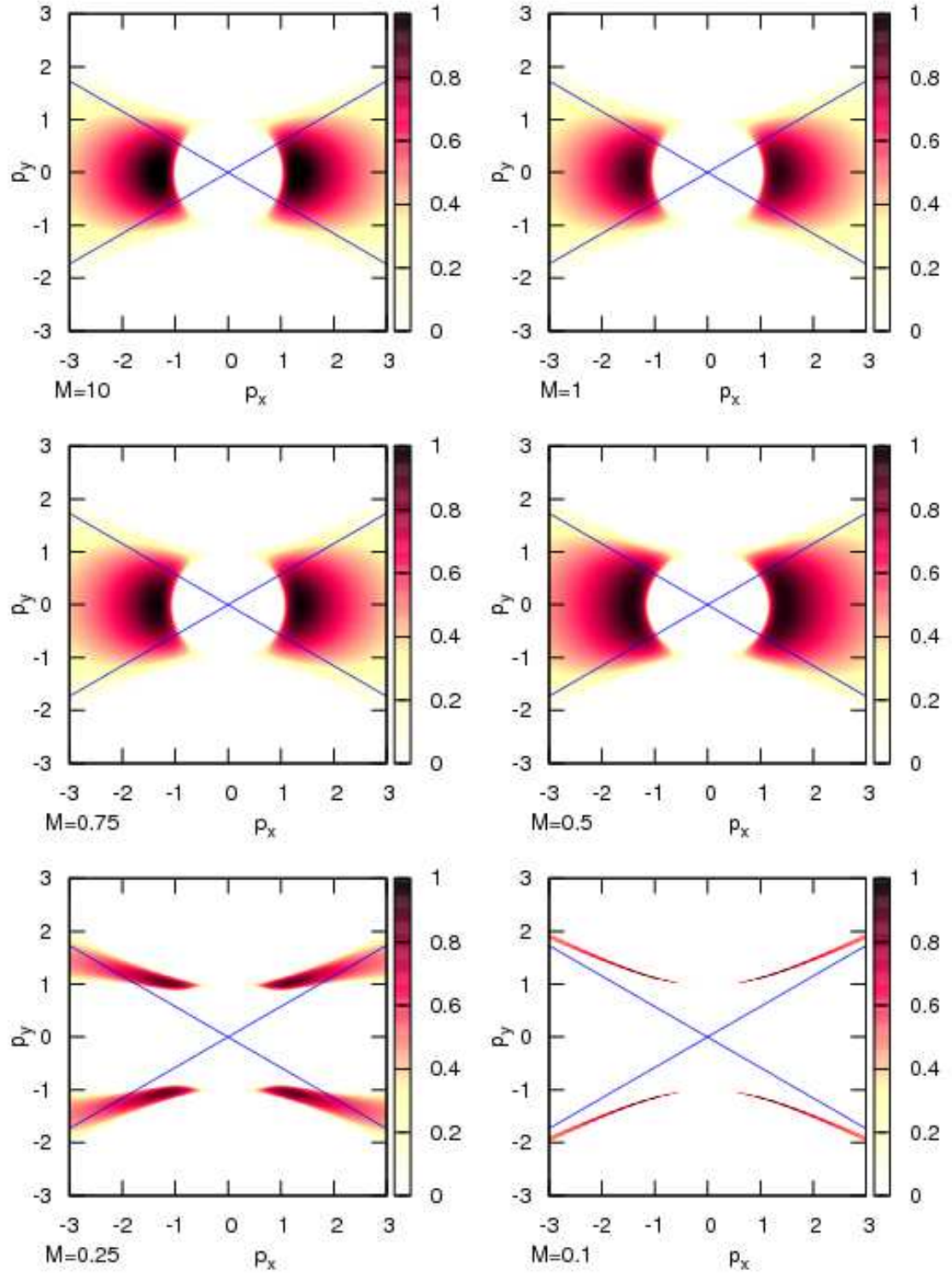


FIG. 11: Same as in Fig. 10 but now for a finite deformation radius, $F = 2$.

ROLE OF THE CARRIER WAVE AMPLITUDE.

We have already mentioned the role of the nonlinearity parameter M , for the most unstable modulation (i.e. zonal for big M and inclined for small M), as well as for the different regimes in the finite F case. Fig. 2 show plots of the instability growthrate as a function of $\mathbf{q} = (q_x, q_y)$ for several different values of M for fixed meridional \mathbf{p} and $F = 0$. In particular we see how the maximum growthrate flips from zonal to off-zonal \mathbf{q} when M is reduced (below see also about the collapse of the unstable region to the resonant curve). Fig. 9 shows plots of the instability growthrate similar to the ones in Fig. 2 but now for finite F . Qualitatively the finite F plots are similar to those obtained for $F = 0$.

Another natural way to visualise the structure of the set of unstable perturbations is to fix the wavevector of the perturbation mode, \mathbf{q} , and plot the instability growth rate as a function of the primary wavevector, \mathbf{p} . Fig. 10 does this, plotting the instability growth rate as a function of $\mathbf{p} = (p_x, p_y)$ for several different values of M with fixed zonal \mathbf{q} and $F = 0$. We see that nonlinearity reduction "eats into" the instability cone, i.e. makes some wavenumbers inside the cone stable. At the same time, the nonlinearity makes some wavenumbers outside the cone unstable. It is important to keep in mind that, even for large M , the maximum growthrate occurs outside of the cone, for the primary wave orientations closer to zonal than to the meridional direction, see Fig. 10 for $M = 10$. This fact is easy to overlook if one considers only the limit $M \rightarrow \infty$ (as it is common in the plasma literature) because, in this limit, the growth rate maximum is for the meridional primary waves. On the other hand, the choice of the primary wave direction is often dictated not by the maximum growthrate of the modulational instability, but by the structure of the primary instability creating the Rossby and drift waves (ITG instability in plasmas and the baroclinic instability in GFD).

Finally, Fig. 11 shows plots of the instability growth rate similar to the ones in Fig. 10 but now for finite F . We again see a qualitatively similar picture to the $F = 0$ case. Note, however, that the global maximum growth rate for large M is now obtained for purely meridional primary waves.

Let us now specially consider the limits $M \gg 1$ and $M \ll 1$.

Limit $M \gg 1$.

The limit of large nonlinearity $M \gg 1$ is a particularly simple and well studied one [1, 2, 18, 20, 21, 26]. As we mentioned before, the β -effect becomes unimportant and, for $F = 0$, this case reduces to instability of Kolmogorov flow in Euler equations (i.e. sinusoidal plane-parallel shear). In this case the most unstable modula-

tion is perpendicular to the carrier wave. The instability criterion reduces to [1]

$$\cos^2 \phi < \left(1 + \frac{q^2}{p^2}\right) / 4,$$

where ϕ is the angle between \mathbf{p} and \mathbf{q} . For the scale separated case, $q \ll p$, this condition describes an "instability cone" [2, 20, 21]

$$|\phi| < \pi/6.$$

Finite deformation radius modifies this cone to a larger instability area [2, 20]

$$F + p_x^2 - 3p_y^2 > 0.$$

We repeat that one has to use the results obtained in the limit $M \rightarrow \infty$ with great caution, because even for large M 's the most unstable primary wave is not predicted correctly in this limit.

Limit $M \ll 1$.

In the limit of weak nonlinearity, $M \ll 1$, the dynamics is completely wave dominated [1]. The nonlinear terms allow waves to interact weakly and exchange energy. Since the nonlinearity is quadratic, wave interactions are triadic (3-wave resonances are allowed by the dispersion relation, Eq. (4)). Any triad of waves having wave-vectors \mathbf{k}_1 , \mathbf{k}_2 and \mathbf{k}_3 interact only if they satisfy the resonance conditions:

$$\mathbf{k}_3 = \mathbf{k}_1 + \mathbf{k}_2 \quad (34)$$

$$\omega(\mathbf{k}_3) = \omega(\mathbf{k}_1) + \omega(\mathbf{k}_2). \quad (35)$$

From Eq.(4), this latter relation gives an implicit equation for the resonant manifold of a given $\mathbf{k}_3 = (k_{3x}, k_{3y})$:

$$\frac{k_{1x}}{k_{1x}^2 + k_{1y}^2 + F} + \frac{k_{3x} - k_{1x}}{(k_{3x} - k_{1x})^2 + (k_{3y} - k_{1y})^2 + F} - \frac{k_{3x}}{k_{3x}^2 + k_{3y}^2 + F} = 0. \quad (36)$$

Because the system is anisotropic, the shape of resonant manifold depends on the direction of \mathbf{k}_3 as shown in Fig. 12.

These resonant manifolds are relevant even for finite nonlinearity since the support of the instability concentrates close to the resonant curves as M is decreased as shown in Fig. 2. Even for $M = 1$ there is a strong connection between the resonant curves and the shape of the set of modulationally unstable perturbations. In fact, Fig. 2 shows two resonant curves corresponding to two resonant triads,

$$\mathbf{k}_1 = \mathbf{p}, \quad \mathbf{k}_2 = \mathbf{q} \quad \text{and} \quad \mathbf{k}_3 = \mathbf{p}_+ = \mathbf{p} + \mathbf{q}$$

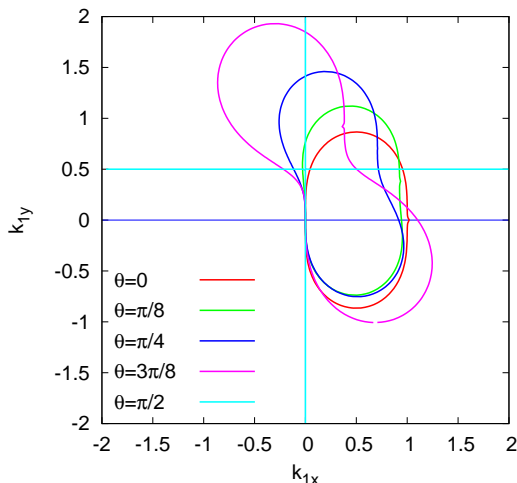


FIG. 12: Shape of the resonant manifold determined by Eq.(36) with $\mathbf{k}_3 = (\cos(\theta), \sin(\theta))$ for several values of θ for the case $F = 0$.

and

$$\mathbf{k}_1 = \mathbf{p}_- = \mathbf{p} - \mathbf{q}, \quad \mathbf{k}_2 = \mathbf{q} \quad \text{and} \quad \mathbf{k}_3 = \mathbf{p}.$$

Out of four wavenumbers in our truncated system, \mathbf{p} , \mathbf{q} , \mathbf{p}_- and \mathbf{p}_+ , three are resonant (or nearly resonant) and the remaining one is non-resonant (\mathbf{p}_- or \mathbf{p}_+). As we mentioned before, this picture is correct in non-degenerate situations, when \mathbf{q} is not zonal. Then for $M \rightarrow 0$ the amplitude of this non-resonant mode in the instability eigenvector tends to zero, so effectively there are only three active modes, and one can use the results obtained above for the 3MT model. In particular, Eq. (15) gives the instability growthrate:

$$\gamma = \frac{|\psi_0| |\mathbf{q} \times \mathbf{p}| \sqrt{(p^2 - q^2)(p_+^2 - p^2)}}{\sqrt{(p_+^2 + F)(q^2 + F)}}. \quad (37)$$

This expression was previously obtained in the case $F = 0$ in [1] based on the 4MT model. One can see that instability of the primary wave occurs if its wavenumber length lies in between of the wavenumber lengths of the waves it decays into, $q < p < p_+$. This condition has a nice dual-cascade interpretation: to decay the wave must be able to transfer its energy to a large scale and its enstrophy to a smaller scale. For $F = 0$, the typical instability growthrate is $\gamma \sim U_0 p$ where $U_0 = p\psi_0$ is the velocity amplitude of the carrier wave [1]. In the large F case, the instability is slowed by the factor F/p^2 (but not arrested).

Another interesting feature of instability for $M \ll 1$ is seen in Fig 10 where we can see that (for fixed zonal q): the unstable region becomes narrow and collapses onto the sides of the "cone", i.e. onto the lines $p_y = \pm p_x/\sqrt{3}$.

This fact can be explained by considering the resonant curve for $q \ll p$ where it behaves as $q_x = -2(p_x p_y/p^4)q_y^3$. For instability, this curve has to pass as close as possible to the vertical (zonal) axis (where we have chosen our \mathbf{q}). Thus, we need to minimize the above coefficient ($p_x p_y/p^4$) (e.g. with respect to p_y for fixed p_x) which immediately gives $p_y = \pm p_x/\sqrt{3}$.

For small M the maximally unstable modulation \mathbf{q} is off-zonal, which may be important for determining the final statistical state of the nonlinear evolution. As we will see later, this state appears to have a predominantly off-zonal component even if the initial modulation is chosen to be zonal.

NONLINEAR EVOLUTION

From now on we study only systems with infinite deformation radius, $F = 0$. To test the linear predictions, and to study the nonlinear evolution, we have performed DNS of the CHM system, Eq. (1), using a standard pseudo-spectral method with resolution up to 1024^2 and hyperviscosity parameters $\nu_n = 4.5e^{-30}$. We solve, in tandem, the 4MT system, (9), and compare it with DNS. Although the 4MT was used as the departure point for the linear stability analysis, it is a fully nonlinear set of equations in its own right. In addition to checking the linear instability predictions against DNS, we will also explore the extent to which the nonlinear dynamics of the 4MT captures the behaviour of the full PDE. In all cases, we choose the initial condition to be along the unstable eigenvector of the 4MT.

Case of Meridional Carrier Wave and Zonal Modulation.

Let us first of all consider the geometry which we dealt with most: purely meridional carrier wave and purely zonal modulation. We choose $\mathbf{p} = (10, 0)$ and $\mathbf{q} = (0, 1)$. A series of frames of the vorticity field for the cases of strong ($M = 10$), medium ($M = 1$) and weak ($M = 0.1$) nonlinearities obtained by DNS are shown in Figs. (13), (14) and (15) respectively. The evolution of the mean zonal velocity $\bar{u}(y)$, averaged over x , obtained from DNS for the same set of nonlinearities is shown in Figs. (16), (17) and (18) respectively for times close to the formation of the jet. Finally, evolution of the amplitude, $|\psi_{\mathbf{q}}|$, of the zonal mode for the same runs is shown in Figs (19), (20) and (21) respectively. For comparison, we also put the corresponding values of $|\psi_{\mathbf{q}}|$ obtained from the 4MT.

Immediately, one can see that the initial stage of evolution agrees very well with the predictions of the linear theory obtained from the 4MT. Moreover, the 4MT works rather well beyond the linear stage, particularly in the

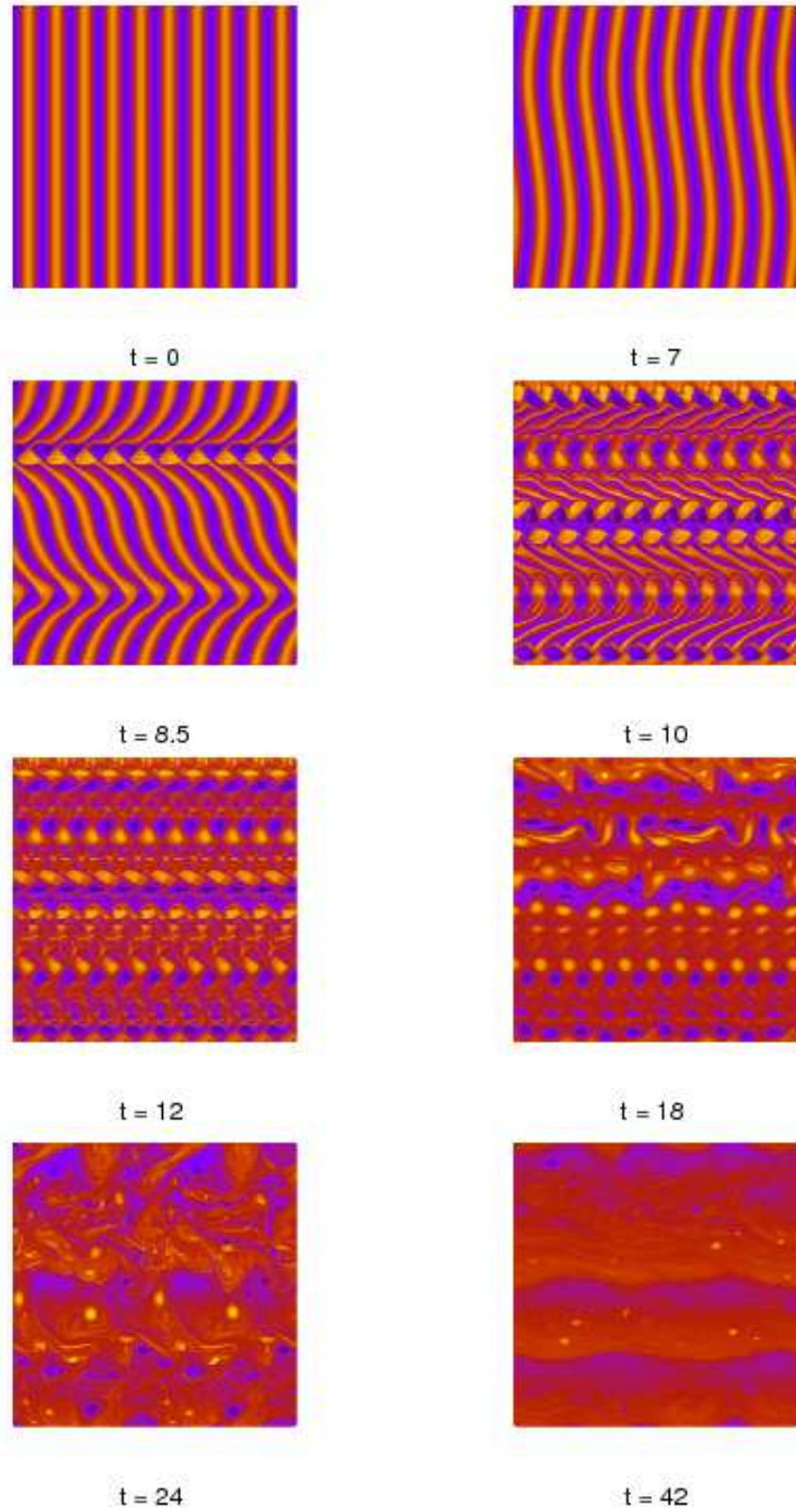


FIG. 13: Vorticity snapshots showing the growth, saturation and transition to turbulence of a zonal perturbation of a meridional carrier wave having $M = 10$.

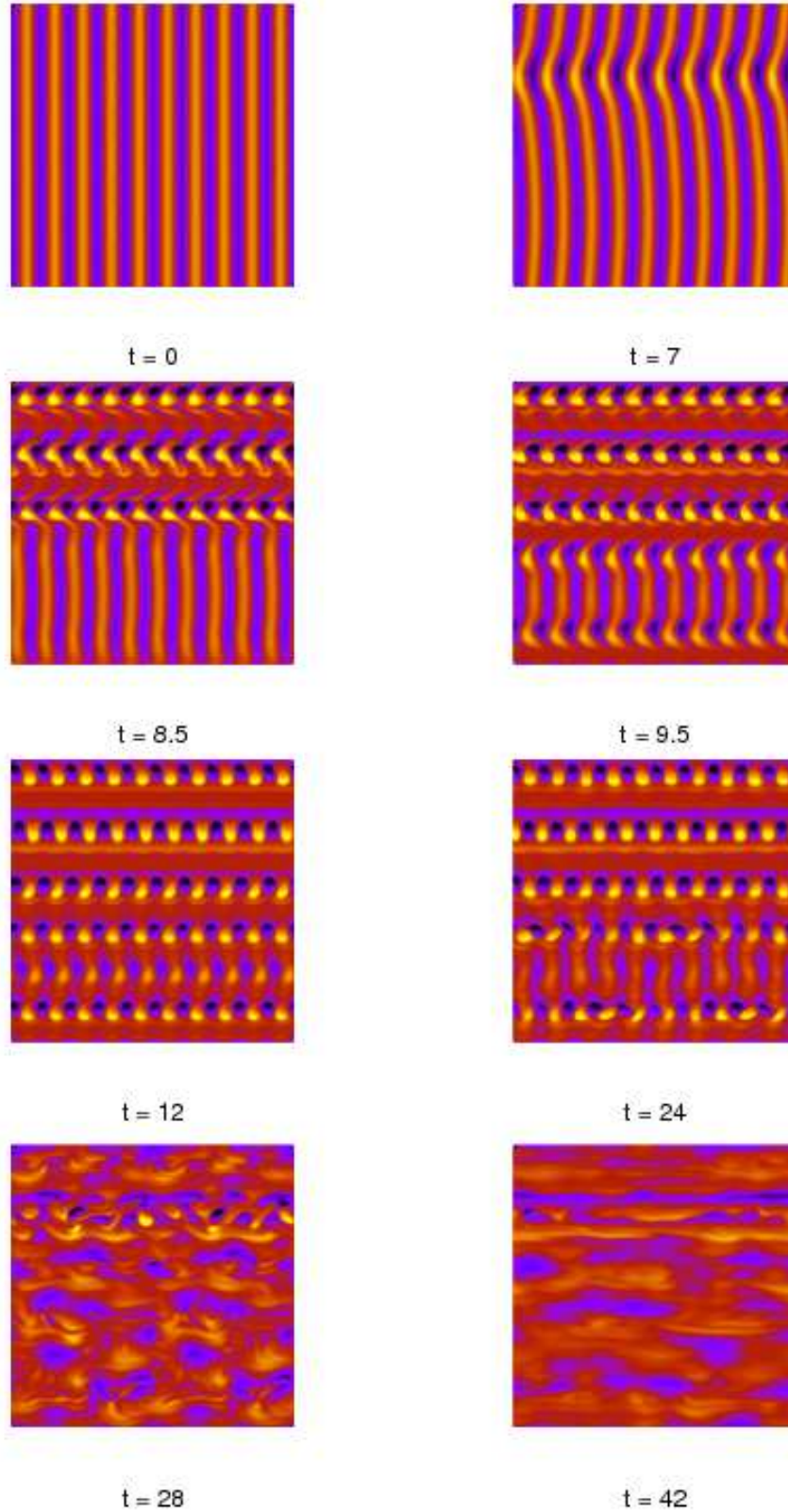


FIG. 14: Vorticity snapshots showing the growth, saturation and transition to turbulence of a zonal perturbation of a meridional carrier wave having $M = 1$.

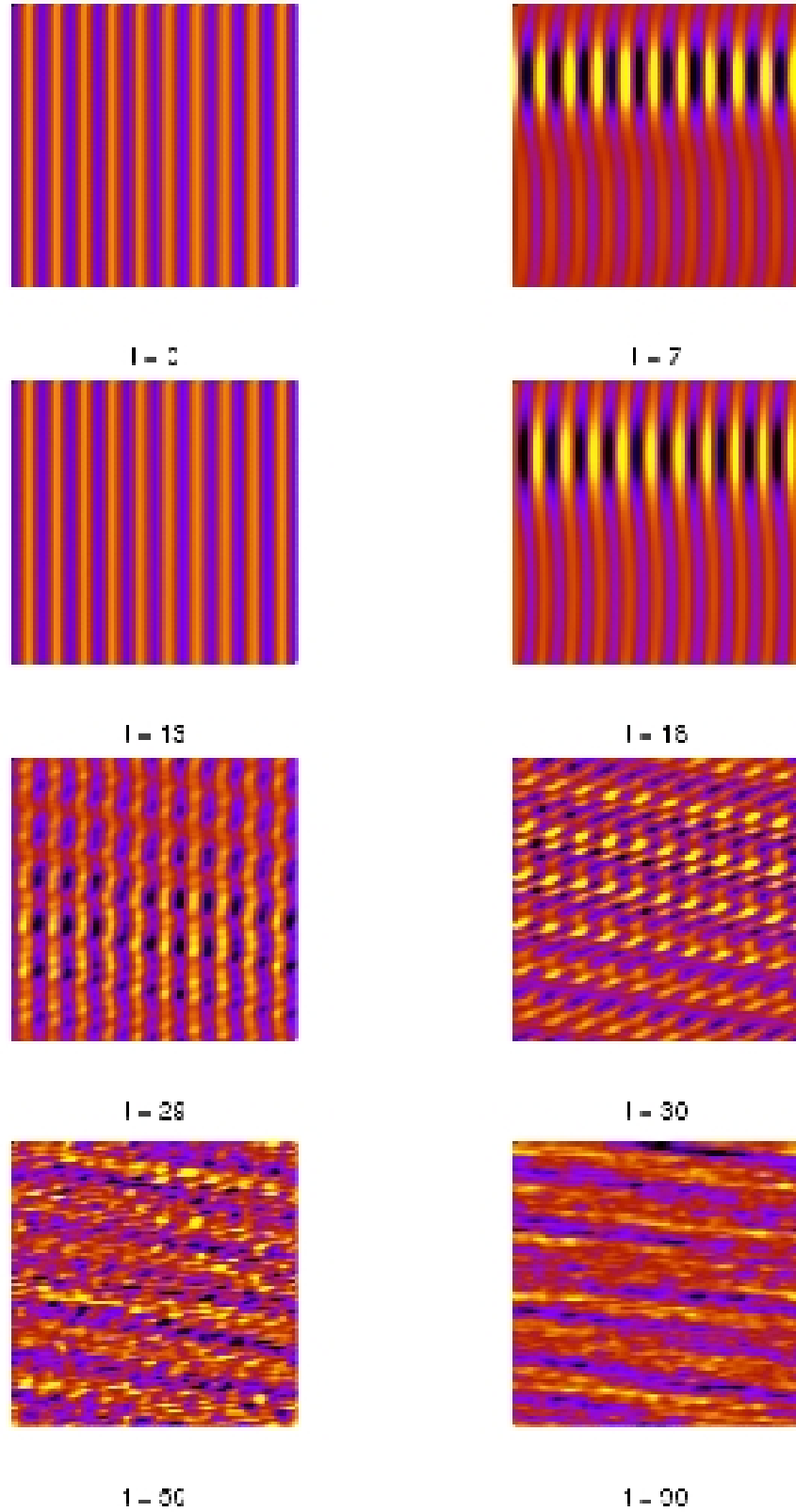
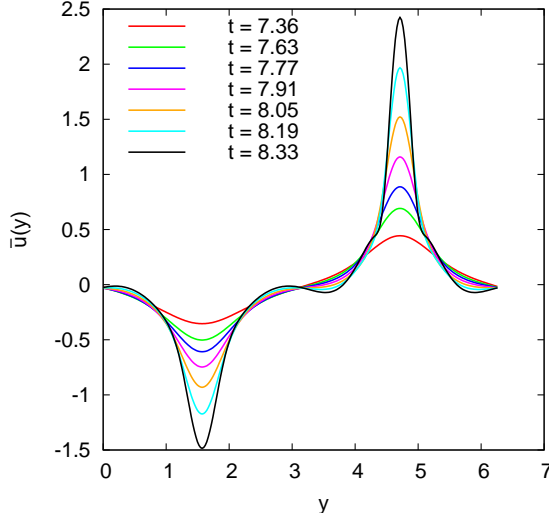
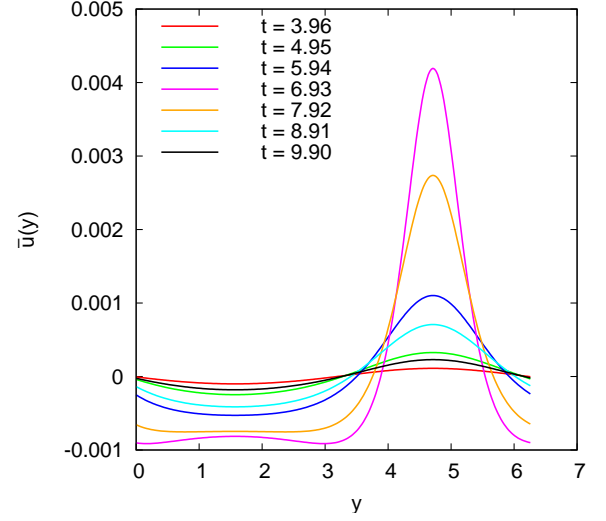
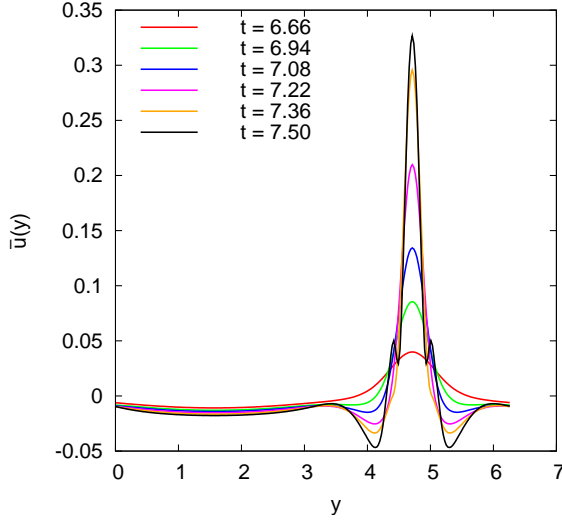


FIG. 15: Vorticity snapshots showing the growth, saturation and transition to turbulence of a zonal perturbation of a meridional carrier wave having $M = 0.1$.

FIG. 16: Mean zonal velocity for $M = 10$ FIG. 18: Mean zonal velocity for $M = 0.1$ FIG. 17: Mean zonal velocity for $M = 1$

$M = 0.1$ case, where the initial growth reverses in agreement with the (periodic) behavior of the four-mode system. For $M = 1$, the system's growth does not reverse, but rather experiences a saturation at the level where the four-mode system reaches maximum and reverses. The most surprising behavior is seen for $M = 10$ where the linear exponential growth continues well beyond the point of reversal of the four-wave system, even though the system is clearly nonlinear at these times and follows a self-similar evolution, see below.

A common feature of the nonlinear saturation stage of the jet growth is self-focusing of the zonal jets which become very narrow with respect to the initial modulation wavelength. This self-focusing cannot be described by the 4MT because such anharmonic jet shapes involve strong contributions from higher harmonics $\mathbf{p} \pm n\mathbf{q}$. For

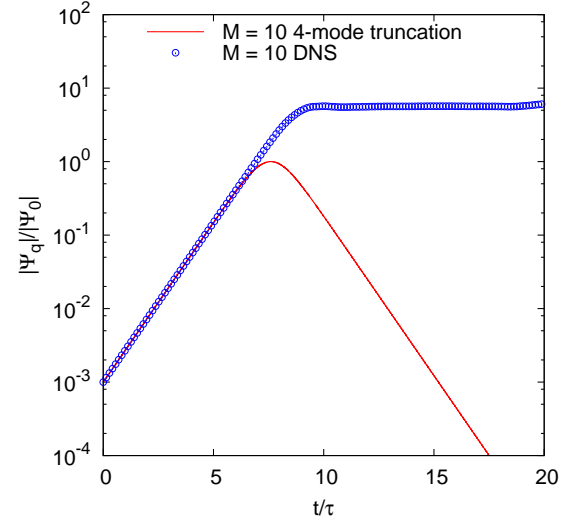


FIG. 19: Growth of the zonal mode \mathbf{q} obtained by DNS and by solving 4MT system for $\mathbf{p} = (10, 0)$ and $\mathbf{q} = (0, 1)$ and for $M = 10$. Time has been scaled by τ (the inverse of the instability growth rate).

large M and $q \ll k$, such jet "pinching" was predicted theoretically in [2] where self-similar solutions were obtained describing a collapse of the jet width. These strong narrow zonal jets are expected to produce transport barriers in the transverse (y) direction, which is important in both fusion plasma and the geophysical contexts.

Figure (22) shows the zonal velocity \bar{u} re-scaled with self-similar variables as $\bar{u}(y, t) = a(t) f(b(t)y)$ in the run with $M = 10$. The self-similar stage occurs in the time interval corresponding to the overshoot in Fig (19), i.e. after the 4MT has reached its maximum but before DNS saturated at a plateau. Empirically, we obtain $a(t) = u_0 e^{\gamma t}$ and $b(t) = e^{1.85t}$. At least during the decade

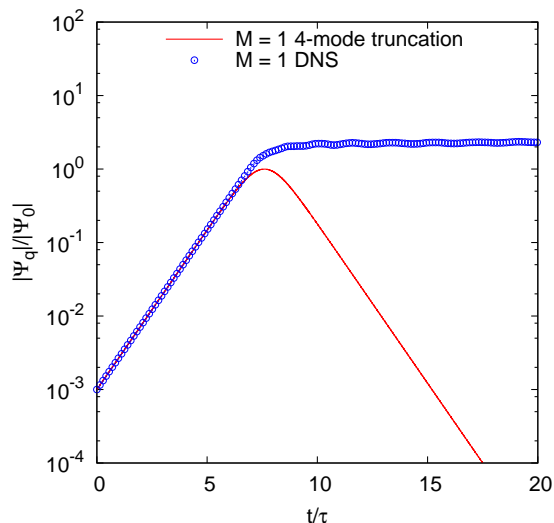


FIG. 20: Same as in Fig. 19 but for $M = 1$

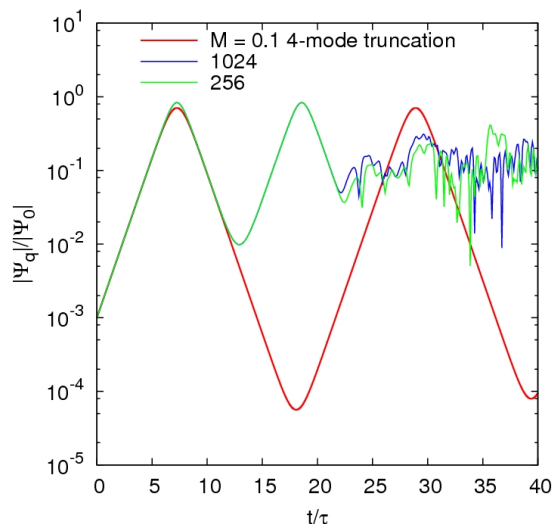


FIG. 21: Same as in Fig. 19 but for $M = 0.1$. DNS results are presented from calculations at two different resolutions to illustrate that the oscillatory dynamics of the zonal mode are not influenced by small scale dissipation.

of amplitude growth observed before pinching occurs, one can see a good evidence of self-similar behaviour and, remarkably, the nonlinear growth at the self-similar stage follows the same exponential law with growthrate γ as on the linear instability stage. Note that the self-similar solutions were obtained in [2] based on the scale separated description and, therefore, the self-similar pinching must stop when the scale separation property breaks down due to the jet narrowing (at which point a roll-up into vortices occurs, see below). In the smaller M runs, the overshoot is absent and the amplitude of the zonal mode decreases after reaching a maximum in correspondence with the solution of the 4MT. The self-focusing is thereby much reduced and the self-similar stage is not clearly observed.

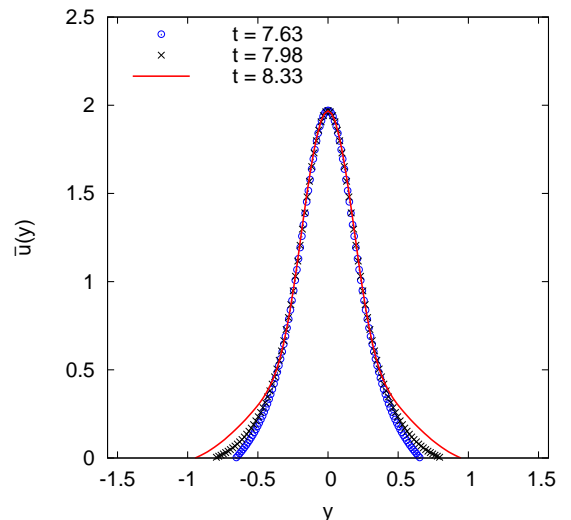


FIG. 22: Zonal velocity $\bar{u}(y)$ re-scaled with self-similar variables: $\bar{u}(y, t) = a(t) f(b(t)y)$ with $a(t) = u_0 e^{\gamma t}$ and $b(t) = e^{1.85t}$ for $M = 10$.

One can also see some qualitative behavior differences for different degrees of nonlinearity M . First of all, we see that the east-west asymmetry is larger for weaker waves, which is seen as asymmetry of the top and bottom halves of the vorticity distributions in Figs. 13, 14 and 15. This is natural considering that for large nonlinearities the beta-effect, which is the cause of the east-west asymmetry, is less important. Further, we see that for large M the nonlinear evolution is vortex dominated and that the vorticity of the initial carrier wave rolls into vortices organized into Karman-like vortex streets. This corresponds to the moment when the jet velocity reaches a plateau in Figs (19) and (20). On the other hand, in the weak wave case $M \ll 1$ one cannot see vortex roll-ups and the dynamics remains wave dominated.

For large nonlinearities, at the final stages the vortex streets break up due to a vortex pairing instability, which is followed by a transition to turbulence. Such turbulence is anisotropic with a pronounced zonal jet component. On the late frames Fig. 13 we can see a well formed potential vorticity staircase structure as described in [37].

For small nonlinearities, $M \ll 1$, the system's nonlinear evolution starts with self-focusing of the primary wave, but this is followed by a quasi-oscillatory behavior where the system returns close to the initial state. This is very well reproduced by the four-wave truncation. The same effect was also noted for the Generalised Hasegawa–Mima model in [34] and in the atmospheric dynamics context in [38]. However, the periodic behavior is not sustained and a transition to an anisotropic turbulent state occurs. It is interesting that the dominant jet structures observed in such a turbulent state are off-zonal. This effect may be connected to the off-zonal “striations” reported for the ocean observations in [7].

We currently regard this connection with some caution since we have not performed any time averaging whereas the ocean striations are sufficiently weak that they only become evident in the averaged data. We hope to investigate this further in future work.

For $M \gtrsim 1$, the vortex streets represent the 2D fine structure of the saturated zonal jets (i.e. at the plateau part of Figs (19) and (20)). Such vortex street configurations are more stable than the plane parallel (x -independent) flows with the same zonal velocity profiles. This can be understood heuristically (see, for example [28], chap. 3) by considering the vortices to impart some eddy viscosity to the mean zonal velocity profile. Recall that stability of the latter is determined by the Rayleigh-Kuo necessary instability condition [39],

$$\partial_{yy}\bar{u}(y) - \beta > 0. \quad (38)$$

Figs (24), (25) and (26) plot the profiles of $\partial_{yy}\bar{u}(y) - \beta$ at different moments in time corresponding to runs with $M = 10$, $M = 1$ and $M = 0.1$ respectively. One can see that in Figs (24) and (25) these profiles cross the x -axis (especially far in the $M = 10$ case) which implies that the zonal flows get stronger than the limiting values implied by the Rayleigh-Kuo condition. We interpret this as a result of a competition between the instability and the jet pinching process. For large M the pinching is self-accelerating (self-similar) and it manages to significantly compress/amplify the unstable jet in the finite time needed for the instability to develop (i.e. the inverse growthrate). On the other hand, in the case $M = 0.1$ the jet strength reaches a maximum and then decreases remaining in the stable range according to the criterion (38).

These results allow us to draw conclusions about the critical value of nonlinearity, $M = M_*$, which separates the two qualitatively different types of behavior: vortex roll-up and saturation vs the oscillatory dynamics, see Figure (23). If the jet strength maximum, as predicted by the 4MT, exceeds the values of Rayleigh-Kuo necessary instability condition (38) then the vortex roll-up occurs and the jet enters into a saturated, relatively long-lived plateau stage. At this moment, the system's behavior starts to depart from the 4MT model. On the other hand, if the jet strength maximum, as predicted by the 4MT, remains below the Rayleigh-Kuo threshold then the system's growth reverses and it follows the 4MT dynamics for longer time.

This simple picture leads to a qualitative physical estimate for M_* and for the saturated velocity of the jet. Let us start with the latter, see Fig. (23).

Since the x -periodicity is preserved, the step of the vortex street is equal to the wavelength of the original carrier wave. The vortices in the stable vortex street are approximately round and the y spacing between the vortices is approximately the same as the x -spacing. Thus, the saturation width of the pinched jet is of order of the

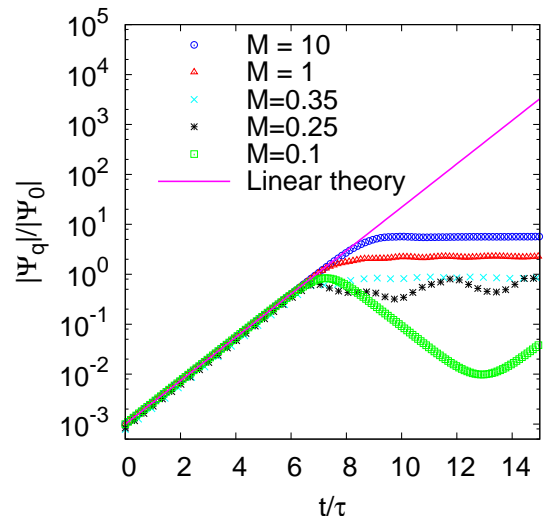


FIG. 23: Growth of zonal perturbations due to modulational instability of a meridional carrier wave having $\mathbf{p} = (10, 0)$ for several different values of M . The amplitude of the zonal mode has been scaled by Ψ_0 and time has been scaled by τ (the inverse of the instability growth rate).

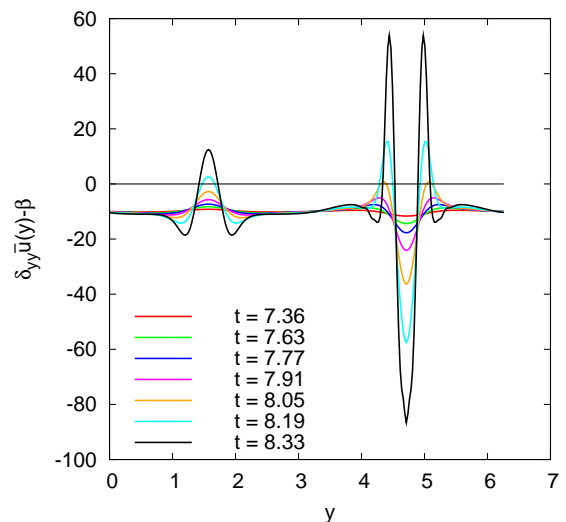
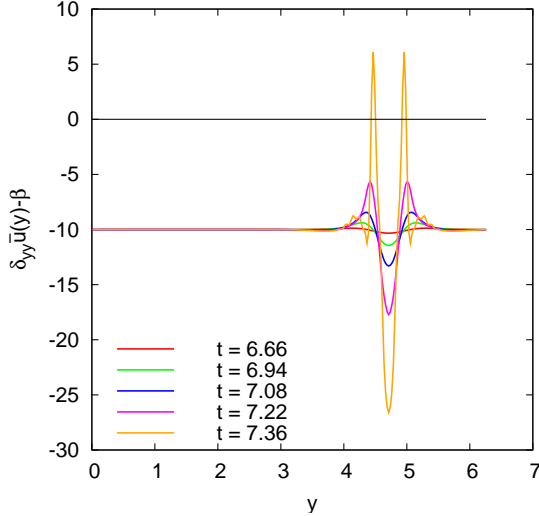
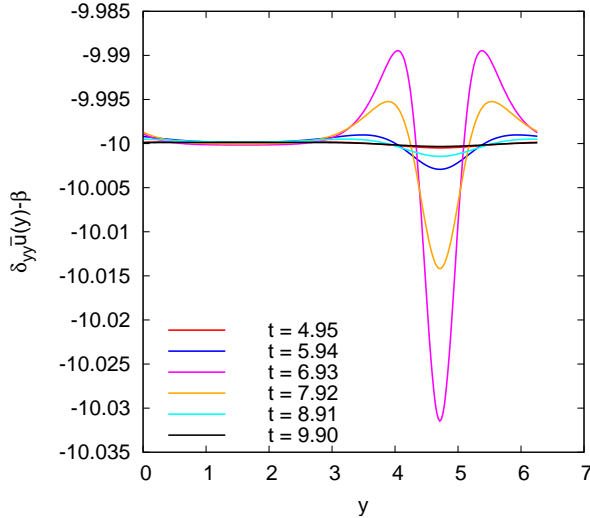


FIG. 24: The Rayleigh-Kuo profiles for $M = 10$

wavelength of the initial carrier wave. Lagrangian conservation of the potential vorticity determines the final saturated amplitude of the jet. Indeed, the same vorticity as in the initial carrier wave rolls into the vortices (the βy part of the potential vorticity does not play much role here since the fluid parcels remain at about the same y 's) and the rest of the vorticity is shed in between of the vortex streets, shredded by shearing and dissipated. Thus, the jet saturation velocity is of the order of the velocity amplitude of the initial carrier wave,

$$\bar{u}_{max} \sim \frac{M\beta}{p^2}. \quad (39)$$

FIG. 25: The Rayleigh-Kuo profiles for $M = 1$ FIG. 26: The Rayleigh-Kuo profiles for $M = 0.1$

This estimate is well confirmed by our numerical results for $M = 1$ and $M = 10$. Indeed, taking values of u_{max} from Figs (16) and (17)) we get

$$\bar{u}_{max} \approx 3 \frac{M\beta}{p^2}. \quad (40)$$

Now, estimating $\partial_{yy}\bar{u}(y)$ as $p^2 u_{max}$ and using (40) we can rewrite the instability condition (38) in a very simple form as

$$M > M_* \sim 1/3.$$

Our numerics show that $M_* \approx 0.25 - 0.35$, see Figure (23). Note that the boundary is not sharp. For $M = 0.25$ the dynamics is definitely wave-dominated, however some elongated fuzzy vortices are still apparent whereas for $M = 0.35$ streets of round vortices are clearly formed with some wave-like oscillations still present.

Case of Meridional Carrier Wave and Off-Zonal Modulation.

Above we considered the case when the carrier wave is purely meridional and the modulation is purely zonal. This geometry is important considering that both the baroclinic instability in GFD and the drift-wave instabilities in plasmas typically have most unstable modes being in the meridional direction. These modes can be considered as an initial condition for the secondary modulational instabilities as it is done in the present paper. At the same time, we have established above that the most unstable modulations for $M > 0.53$ are zonal.

On the other hand, for low M the most unstable modulations are off-zonal. This, in our opinion, is the reason why the final statistical state in the system in the $M = 0.1$ simulation showed presence of off-zonal anisotropic flows even though the initial modulation was purely zonal. Moreover, it is quite likely that in such weakly-nonlinear cases the system will pick the modulation which is off-zonal already at the initial moments.

Thus, here we will consider a case with $M = 0.1$ where we start with purely meridional carrier wave, $\mathbf{p} = (10, 0)$ and with the modulation wavevector corresponding to the fastest growing mode in this case, namely $\mathbf{q} = (9, 6)$. Corresponding numerical results for this case are shown in Fig. (27) (vorticity snapshots) and Fig. (5) (evolution of the q -mode amplitude $|\psi_q|$ and respective results obtained from simulating the 4MT and 3MT models).

First of all, as in all previous cases, we see good agreement of the initial evolution with predictions for the linear instability obtained based on the 4MT and the 3MT models. Moreover, we see that the 4MT and the 3MT in this case qualitatively describe the nonlinear behavior too. Namely, like in the four-mode system, we see oscillatory behavior, even though the oscillations appear to be irregular. However, these irregular oscillations are clearly non-turbulent, as one can see from the vorticity frames in Fig. (27) which shows quite a regular pattern even at $t = 100$ (in the units of the inverse instability growthrate), - by which time the respective $M = 0.1$ system with zonal \mathbf{q} is completely turbulent, see Fig. 15. Another way to see that the dynamics are regular in this case is to look at the 2D k -spectra shown in Fig. (28). At $t = 0$, the only excited modes are the carrier wave \mathbf{p} , modulation \mathbf{q} and two satellites $\mathbf{p} \pm \mathbf{q}$: these modes are marked by bold symbols in Fig (28). At $t = 60$ one can see a regular "crystalline" structure corresponding to a discrete set of nodes $n\mathbf{p} + m\mathbf{v}$ (with integer values of m and n) with energy within 1% of the initial carrier wave energy. Transition to turbulence does eventually occur after a very long time, and the turbulent state does exhibit off-zonal striations similar to the respective $M = 0.1$ system with zonal initial modulations \mathbf{q} .

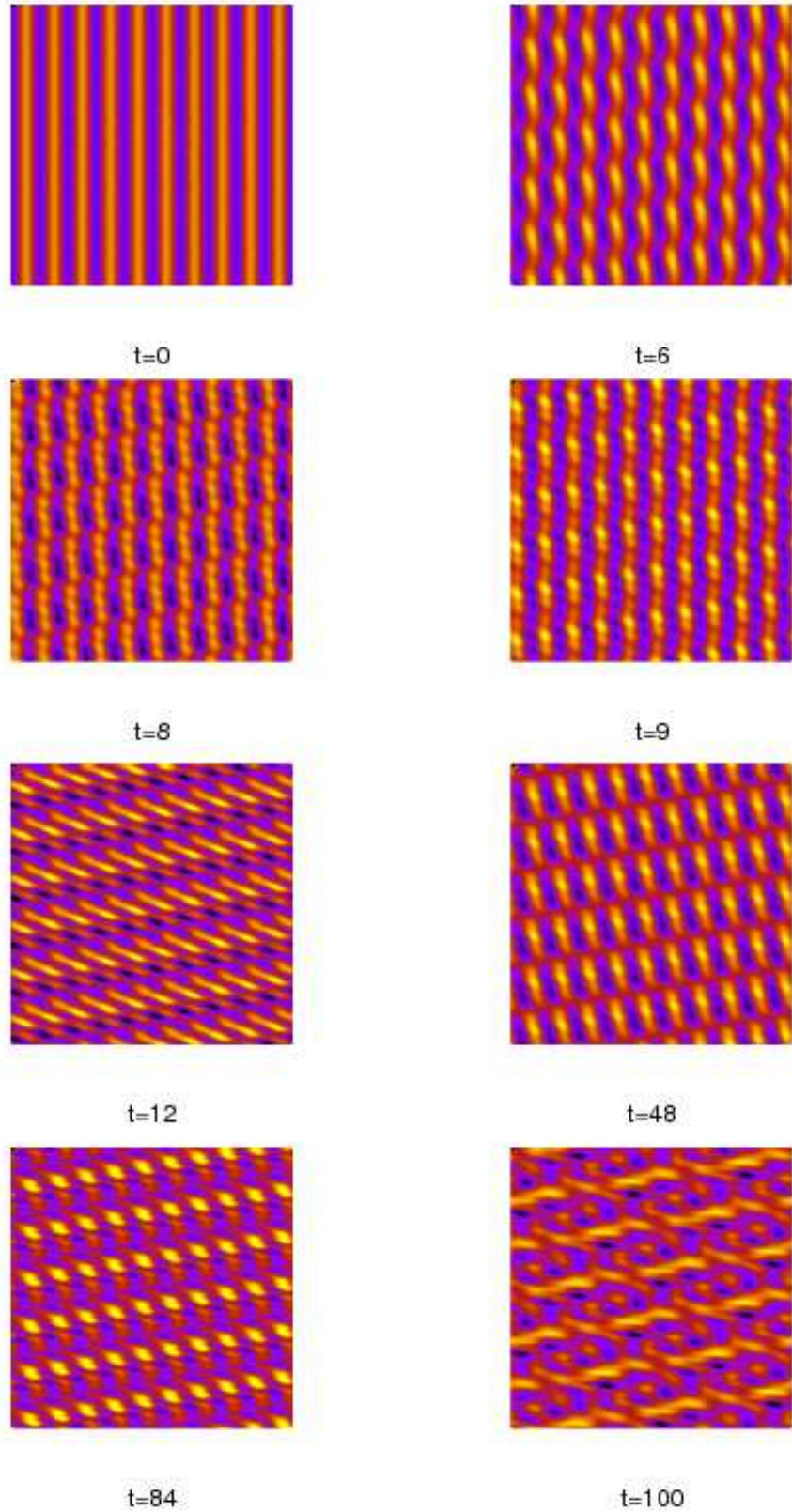


FIG. 27: Vorticity snapshots showing the growth, saturation and transition to turbulence of an off-zonal perturbation of a meridional carrier wave having $M = 0.1$.

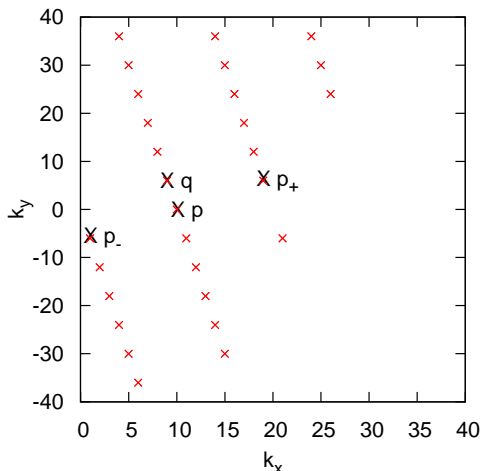


FIG. 28: Excited modes at $t = 60$ with energy within 1% of the energy of the initial perturbation in run with for $q = (9, 6)$, $M = 0.1$.

STABLE CASE

Above we considered in detail various situations where the linear theory based on the 4MT model predicts instability. We have also investigated the linearly stable case.

For small M the zonal mode in the modulationally stable case behaves as expected, following the 4MT theory without growth of the mode. In this case, deviations from the 4MT are tiny, hence we omitted the corresponding graph. For $M \gg 1$, the situation is more interesting. Fig. 29 shows the evolution of the zonal mode for the run with $\mathbf{p} = (8, 6)$ and $\mathbf{q} = (0, 1)$ and for $M = 10$ which corresponds to a linearly stable configuration within the 4MT model. We see agreement with the 4MT stability prediction at early times, i.e. the zonal mode is not growing in Fig. 29 for $t \lesssim 1$. However, after about one timescale the zonal mode quickly breaks into growth, increasing (more or less exponentially) by two orders of magnitude. Hence, the 4MT instability criterion must be used with caution if $M \gg 1$. Further, for $M \gg 1$ stable case Manin and Nazarenko [2] predicted zonal velocity profile steepening for and this is evident in Fig. 30 where the initial sinusoidal profile develops into a triangular Burger's shock-type profile.

SUMMARY AND CONCLUSIONS

In this paper we dealt with the theory and numerical simulations of the modulational instability of the Rossby/drift waves described by the CHM model. We

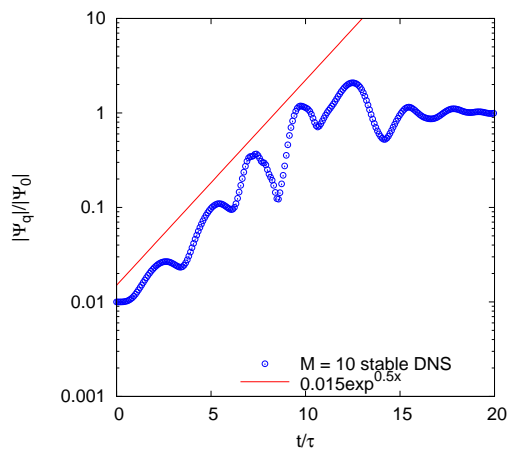


FIG. 29: Growth of the zonal mode \mathbf{q} obtained by DNS for $\mathbf{p} = (8, 6)$ and $\mathbf{q} = (0, 1)$ and for $M = 10$.

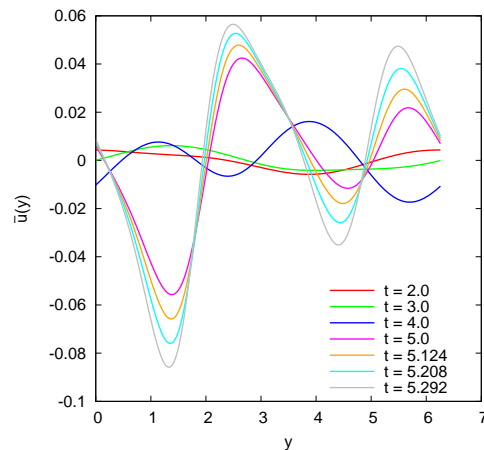


FIG. 30: Mean zonal velocity profile for the stable configuration $\mathbf{p} = (8, 6)$, $\mathbf{q} = (0, 1)$ and $M = 10$.

have revisited the linear theory of Gill [1] using the 4-mode truncation and emphasised the role of the carrier wave amplitude/nonlinearity, the role of the deformation radius and the role of resonant wave interactions in the case of weakly nonlinear carrier wave. We found a change of the most unstable modulation from zonal to off-zonal when the carrier wave nonlinearity parameter M falls below a critical value, $M > 0.53$. This latter effect may be important for understanding the recent ocean observation of off-zonal jet striations [7]. It is also a likely mechanism for generation of off-zonal random jets in our numerical simulations at the late development stages of the modulational instability for $M = 0.1$ case.

We established how the modulational instability relates to the decay instability obtained within the 3-mode truncation in order to clarify the question whether the dominant nonlinear mechanism of the modulational instability is three-wave or four-wave. The 3MT works very well for low nonlinearities M when the carrier wave and

the modulation belong to the same resonant triad which is non-degenerate, i.e. when it does not include wavevectors too close to $k = 0$ point where the two branches of the resonant curve intersect. This excludes the most popular choice of purely zonal modulations, for which 3MT appears to be a bad model. On the other hand, 4MT is more general and it works very well for small nonlinearities M including the case of the purely zonal modulations. Moreover, 4MT also works well for the initial evolution in the strongly nonlinear cases, $M \gtrsim 1$, including the linear growth stage and the prediction of the critical nonlinearity M_* for which transition from the saturated to the oscillatory nonlinear regimes is observed.

We checked the solutions of the truncated system against DNS and concluded that it is sufficient to predict both the linear instability and the early nonlinear evolution of this instability. We showed that DNS agrees very well with the linear predictions in all cases. In many cases, particularly for small M and in the stable configurations, the four-wave truncation predicts quite well the early and intermediate nonlinear evolution phases. The nonlinear evolution for small M 's is characterized by dominant wave dynamics, whereas for large M 's the nonlinear evolution leads to rolling up of the carrier wave vorticity into Karman-like vortex streets. Such hydrodynamic vortices behave very differently from waves, and it is precisely at the moment of roll-up that the full system's evolution strongly diverges from the prediction of the four-wave truncation. After the roll-up the full system enters into a saturated quasi-stable state which persists for a relatively long time but eventually decays due to presence of hyper-viscosity. On other hand, the corresponding four-wave system keeps going through an infinite sequence of nonlinear oscillations. If M is small and the roll-ups do not occur (or are delayed) the full system may follow its four-wave counterpart for much longer: its initial growth can reverse and may exhibit the nonlinear oscillations associated with the 4MT.

Finally, we would like to emphasize two physical effects that can be important for both plasma and GFD systems. For $M \gtrsim 1$ we observe the formation of stable, narrow zonal jets, in agreement with earlier theoretical predictions of [2]. As we mentioned, these jets are more stable than one would expect based on the Rayleigh-Kuo criterion alone because their 2D structure consists of stable vortex streets. Such narrow jets represent very effective transport barriers which may be responsible for the LH transitions in tokamaks. Indeed, narrowness of the jet causes characteristic pedestal-like radial profiles of the particles and energy typically seen in tokamaks during H-mode, i.e. the narrow jet provides a thin "insulation" layer (called internal transport barrier) which keeps the particle and energy densities significantly higher inside. The second physical effect we would like to mention occurs at low nonlinearities M . This is the fact that the system tends to select the states with somewhat off-zonal jet

structures. This tendency to favour the off-zonal structures is seen already on the level of the linear analysis, where as we showed the most unstable modulation changes from zonal to off-zonal when the nonlinearity is reduced. Possibly, this mechanism can explain recent ocean observation of off-zonal jet striations [7] (note that the nonlinearity of the ocean Rossby waves in these situations is likely to be rather low).

In future, it would be interesting to study in more detail how the transport properties are affected by both zonal and off-zonal jets that arise in the strongly and weakly nonlinear cases respectively. In particular, it would be interesting to see how different are the transport barriers provided by coherent vortex streets from the barriers provided by random jets at the later stages. It would also be interesting to study situations where a broad spectrum of modulations is present initially and, in particular, to verify that the system selects the most unstable one. If the carrier wave spectrum is not narrow it would be of interest to study when the modulational instability wins over the inverse cascade mechanism.

* Electronic address: connaughtonc@gmail.com

† Electronic address: balu@lanl.gov

‡ Electronic address: S.V.Nazarenko@warwick.ac.uk

§ Electronic address: B.E.Quinn@warwick.ac.uk

- [1] A. E. Gill, *Geophys. Fluid Dyn.* **6**, 29 (1974).
- [2] D. Y. Manin and S. V. Nazarenko, *Phys. Fluids* **6**, 1158 (1994).
- [3] A. A. Simon, *Icarus* **141**, 29 (1999).
- [4] A. Sanchez-Lavega, J. F. Rojas, and P. V. Sada, *Icarus* **147**, 405 (2000).
- [5] B. Galperin, H. Nakano, H.-P. Huang, and S. Sukoriansky, *Geophys. Res. Lett.* **31**, L13303 (2004).
- [6] J. M. Lewis, *Bull. Amer. Met. Soc.* **79** (1988).
- [7] N. A. Maximenko, O. V. Melnichenko, P. P. Niiler, and H. Sasaki, *Geophys. Res. Lett.* **35**, L08603 (2008).
- [8] I. N. James, *J. Atmo. Sci.* **44**, 3710 (1987).
- [9] P. H. Diamond, S.-I. Itoh, K. Itoh, and T. S. Hahm, *Plasma Phys. Control. Fusion* **47**, R35 (2005).
- [10] A. M. Balk, S. V. Nazarenko, and V. E. Zakharov, *Phys. Lett. A* **146**, 217 (1990).
- [11] A. M. Balk, S. V. Nazarenko, and V. E. Zakharov, *Sov. Phys. - JETP* **71**, 249 (1990).
- [12] F. Wagner, G. Becker, K. Behringer, D. Campbell, A. Eberhagen, W. Engelhardt, G. Fussmann, O. Gehre, J. Gernhardt, G. v. Gierke, et al., *Phys. Rev. Lett.* **49**, 1408 (1982).
- [13] R. H. Kraichnan, *Phys. Fluids* **10**, 1417 (1967).
- [14] A. M. Balk, S. V. Nazarenko, and V. E. Zakharov, *Phys. Lett. A* **152**, 276 (1991).
- [15] A. M. Balk, *Phys. Lett. A* **155**, 20 (1991).
- [16] A. M. Balk, *SIAM Review* **39**, 68 (1997).
- [17] S. V. Nazarenko and B. E. Quinn, *ArXiv e-prints* (2009), 0905.1314.
- [18] E. N. Lorentz, *J. Atmo. Sci.* **29**, 258 (1972).
- [19] K. K. Mima and Y. C. Lee, *Phys. Fluids* **23**, 105 (1980).

- [20] A. I. Smolyakov, P. H. Diamond, and V. I. Shevchenko, *Phys. Plasmas* **7**, 1349 (2000).
- [21] O. Onishchenko, O. Pokhotelov, R. Sagdeev, P. Shukla, and L. Stenflo, *Nonlin. Proc. Geophys.* **11**, 241 (2004).
- [22] A. I. Smolyakov and S. I. Krasheninnikov, *Phys. Plasmas* **15**, 072302 (2008).
- [23] T. Benjamin and J. Feir, *J. Fluid Mech.* **27**, 417 (1967).
- [24] M. Onorato, A. R. Osborne, M. Serio, and S. Bertone, *Phys. Rev. Lett.* **86**, 5831 (2001).
- [25] P. A. E. M. Janssen, *J. Phys. Ocean.* p. 863 (2003).
- [26] V. I. Arnold and L. D. Meshalkin, *Usp. Mat. Nauk* **15**, 247 (1960).
- [27] Z. Sagdeev and A. A. Galeev, *Nonlinear Plasma Theory* (Benjamin, New York, 1969).
- [28] J. C. McWilliams, *Fundamentals of Geophysical Fluid Dynamics* (Cambridge University Press, 2006).
- [29] J. G. Charney, *J. Meteor.* **6**, 371 (1949).
- [30] A. Hasegawa and K. Mima, *Phys. Fluids* **21**, 87 (1978).
- [31] L. I. Rudakov and R. Z. Sagdeev, *Sov. Phys. Dokl.* **6**, 415 (1961).
- [32] E. Kartashova and V. S. L'vov, *Phys. Rev. Lett.* **98**, 198501 (2007).
- [33] M. D. Bustamante and E. Kartashova, *Europhys. Lett.* **85**, 34002 (2009).
- [34] G. Manfredi, C. M. Roach, and R. O. Denby, *Plasma Phys. Control. Fusion* **43**, 825 (2001).
- [35] P. Rhines, *J. Fluid Mech.* **69**, 417 (1975).
- [36] C. Connaughton, S. Nazarenko, and A. Pushkarev, *Phys. Rev. E* **63**, 046306 (2001).
- [37] D. G. Dritschel and M. E. McIntyre, *J. Atmos. Sci.* **65**, 855 (2008).
- [38] A. C. Mahanti, *Arch. Met. Geoph. Biokl., Ser. A* **30**, 211 (1981).
- [39] H. L. Kuo, *J. Meteor.* **6**, 105 (1949).